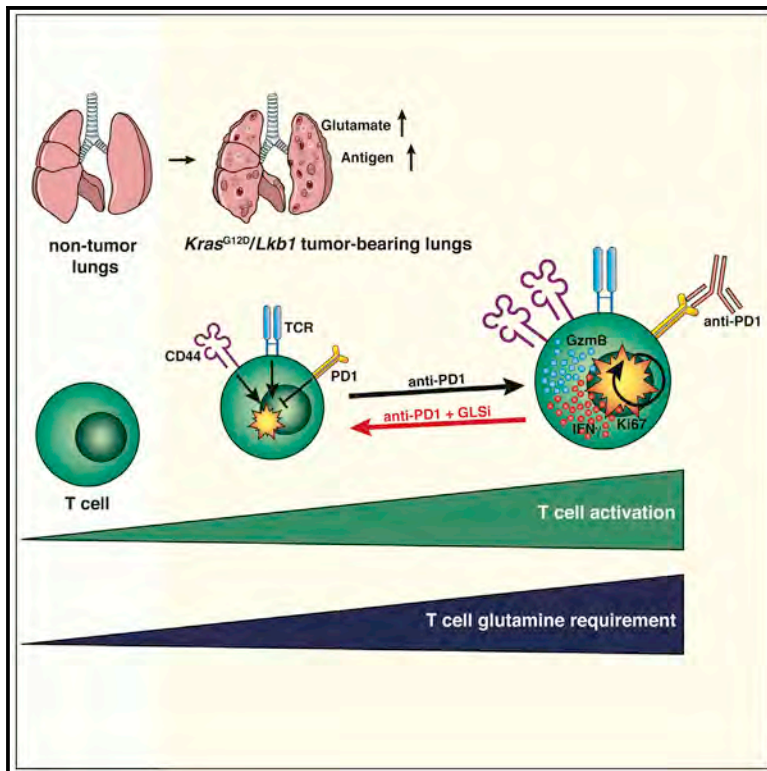


Cell Metabolism

Glutaminase inhibition impairs CD8 T cell activation in *STK11*-/*Lkb1*-deficient lung cancer

Graphical abstract



Authors

Sarah A. Best, Patrick M. Gubser, Shalini Sethumadhavan, ..., Axel Kallies, Gillian Kingsbury, Kate D. Sutherland

Correspondence

best@wehi.edu.au (S.A.B.), sutherland.k@wehi.edu.au (K.D.S.)

In brief

Best et al. investigated the metabolism of *KRAS*-mutant lung adenocarcinoma and found that *STK11/Lkb1* co-mutation (KL) results in increased glutamate and glutaminase. Glutaminase inhibition (CB-839) combined with immunotherapy (anti-PD1) in the KL model was not efficacious *in vivo*, resulting in CD8 T cells with reduced clonal expansion and cytotoxicity.

Highlights

- *Kras* co-mutations alter the metabolic profile of lung adenocarcinoma
- Glutaminase (Gls1) activity in KL tumors increases glutamate in the TME
- Glutaminase inhibition combined with immunotherapy inhibits TCR clonotype expansion
- Activated CD8 T cells are dependent on available glutamine and glutaminase activity



Article

Glutaminase inhibition impairs CD8 T cell activation in *STK11*-/*Lkb1*-deficient lung cancer

Sarah A. Best,^{1,2,*} Patrick M. Gubser,³ Shalini Sethumadhavan,^{4,8} Ariena Kersbergen,^{1,9} Yashira L. Negrón Abril,^{4,10} Joshua Goldford,^{4,11} Katherine Sellers,^{4,12} Waruni Abeysekera,^{2,5} Alexandra L. Garnham,^{2,5} Jackson A. McDonald,^{1,2} Clare E. Weeden,^{2,6,13} Dovile Anderson,⁷ David Pirman,⁴ Thomas P. Roddy,^{4,14} Darren J. Creek,⁷ Axel Kallies,³ Gillian Kingsbury,^{4,15} and Kate D. Sutherland^{1,2,16,*}

¹ACRF Cancer Biology and Stem Cells Division, The Walter and Eliza Hall Institute of Medical Research, Parkville, VIC, Australia

²Department of Medical Biology, University of Melbourne, Parkville, VIC, Australia

³Department of Microbiology and Immunology, The Peter Doherty Institute for Infection and Immunity, University of Melbourne, Melbourne, Australia

⁴Agios Pharmaceuticals, Cambridge, MA, USA

⁵Bioinformatics Division, The Walter and Eliza Hall Institute of Medical Research, Parkville, VIC, Australia

⁶Personalised Oncology Division, The Walter and Eliza Hall Institute of Medical Research, Parkville, VIC, Australia

⁷Monash Proteomics and Metabolomics Facility, Monash Institute of Pharmaceutical Sciences, Monash University, Parkville, VIC, Australia

⁸Present address: Cygnal Therapeutics, Watertown, MA, USA

⁹Present address: Peter MacCallum Cancer Centre, Melbourne, VIC, Australia

¹⁰Present address: Caris Life Sciences, Phoenix, AZ, USA

¹¹Present address: Physics of Living Systems, Massachusetts Institute of Technology, Cambridge, MA, USA

¹²Present address: Rheos Medicines Inc., Cambridge, MA, USA

¹³Present address: The Francis Crick Institute, London, UK

¹⁴Present address: Atavistik Bio, Cambridge, MA, USA

¹⁵Present address: ManaT Bio Inc., Baltimore, MD, USA

¹⁶Lead contact

*Correspondence: best@wehi.edu.au (S.A.B.), sutherland.k@wehi.edu.au (K.D.S.)

<https://doi.org/10.1016/j.cmet.2022.04.003>

SUMMARY

The tumor microenvironment (TME) contains a rich source of nutrients that sustains cell growth and facilitate tumor development. Glucose and glutamine in the TME are essential for the development and activation of effector T cells that exert antitumor function. Immunotherapy unleashes T cell antitumor function, and although many solid tumors respond well, a significant proportion of patients do not benefit. In patients with *KRAS*-mutant lung adenocarcinoma, *KEAP1* and *STK11/Lkb1* co-mutations are associated with impaired response to immunotherapy. To investigate the metabolic and immune microenvironment of *KRAS*-mutant lung adenocarcinoma, we generated murine models that reflect the *KEAP1* and *STK11/Lkb1* mutational landscape in these patients. Here, we show increased glutamate abundance in the *Lkb1*-deficient TME associated with CD8 T cell activation in response to anti-PD1. Combination treatment with the glutaminase inhibitor CB-839 inhibited clonal expansion and activation of CD8 T cells. Thus, glutaminase inhibition negatively impacts CD8 T cells activated by anti-PD1 immunotherapy.

INTRODUCTION

KRAS is the most frequently altered oncogene in lung adenocarcinoma and, until recently (Hallin et al., 2020), has been considered an undruggable protein (Papke and Der, 2017). To better understand *KRAS*-mutant lung adenocarcinoma, the underlying genetic landscape of alterations in frequently co-occurring tumor suppressors *TP53* (*KRAS/TP53*), *CDKN2A* (*KRAS/CDKN2A*), *KEAP1*, and *STK11/Lkb1* (*KRAS/STK11*) have been interrogated, identifying distinct subsets of *KRAS*-mutant disease (Skoulidis et al., 2015). Although *KEAP1* and *STK11/Lkb1* alterations coexist in a single subset (*KRAS/STK11*), a similar proportion of patients with *KRAS*-mutation exclusively harbor either *KEAP1* or *STK11*/

Lkb1 mutation (co-mutated: ~10%; *KEAP1* only: ~5%; *STK11* only: ~10%) (Best et al., 2019; Wohlhieter et al., 2020). Therefore, a greater understanding of the molecular characteristics of these refined subsets is crucial to better understand the patient disease.

Immunotherapy based on PD1/PD-L1 axis checkpoint blockade unleashes CD8 T cells, enabling robust antitumor responses. In non-small cell lung cancer (NSCLC), only 20% patients receive benefit from immunotherapy treatment, a surprisingly low number, given the high mutational burden and immune infiltration observed in lung cancers (Chalmers et al., 2017; Rizvi et al., 2015). This has ignited interest into understanding the mechanisms underlying antitumor immunity in lung cancer. Early analyses of the *KRAS/STK11* subset revealed reduced immune



infiltration (Skoulidis et al., 2015) and poorer response to immunotherapy (Cristescu et al., 2018; Skoulidis et al., 2018) compared with *STK11* wild-type counterparts. Reclassification of the *KRAS/STK11* subset by *KEAP1*- in addition to *STK11/Lkb1* mutation has further revealed that *STK11*-mutant tumors have reduced PD-L1 tumor expression (Lamberti et al., 2020) and poor response to anti-PD-L1 (atezolizumab) (Singh et al., 2021). These recent findings highlight the importance of understanding the response to immunotherapy in distinct genetic environments in the preclinical setting.

The switch from oxidative phosphorylation to glycolytic metabolism is critical to the activation of T cells (Wang et al., 2011). In the tumor microenvironment (TME), glucose and glutamine (Gln) are in high demand from both tumor cells and infiltrating immune cells (Carr et al., 2010; Momcilovic et al., 2018; Sinclair et al., 2013). Indeed, *KEAP1*-mutant tumor cells, which have an active NRF2 pathway (Best and Sutherland, 2018), display elevated expression of the Gln importer SLC1A5 (Romero et al., 2017) and rely on glutaminolysis to exchange glutamate (Glu) for cystine via the antiporter xCT (SLC3A2/SLC7A11) (Sayin et al., 2017). Cystine is critical in the production of glutathione (GSH), a key antioxidant generated in the NRF2 pathway (DeNicola et al., 2015). Therefore, *KEAP1*-mutant NSCLC cell lines are reliant on Gln in the culture medium and are sensitive to glutaminase (Gls1) inhibition (CB-839) (Galan-Cobo et al., 2019; Gross et al., 2014; Romero et al., 2017; Sayin et al., 2017). To date, NSCLC studies have been performed *in vitro* using cell lines with co-mutation in *KEAP1* and *STK11/Lkb1*. Thus, the genetic dependencies of Gln and sensitivity to glutaminase inhibition is yet to be fully explored in NSCLC with either *KEAP1* or *STK11/Lkb1* genetic alteration and an intact TME.

It is speculated that *KEAP1*-mutant tumors would import high quantities of Gln from the TME, thereby limiting Gln availability for infiltrating T cells and thus blocking their ability to activate (Chang et al., 2015). Therefore, the combination of glutaminase inhibition and immunotherapy has been speculated to be beneficial in this environment (Byun et al., 2020). Here, we employed genetically engineered mouse models (GEMMs) to dissect the heterogeneity of *KEAP1* and *STK11/Lkb1* co-mutations in autochthonous *KRAS*-mutant lung adenocarcinoma. We identified distinct differences between the metabolic environments of *Keap1*- compared with *Lkb1*-deficient tumors that likely contribute to differential responses of CD8 T cells to anti-PD1 treatment. However, contrary to the hypothesis that glutaminase inhibition and immunotherapy would synergize in such an environment, we found that the cytotoxic activation of CD8 T cells was impaired, inhibiting their antitumor capabilities. Thus, utilizing autochthonous murine lung cancer models, we demonstrate that glutaminase inhibition fails to bolster the immune response elicited when combined with immunotherapy.

RESULTS

Kras^{G12D} co-mutation dictates the metabolic environment of lung adenocarcinoma

To characterize the impact of *KRAS* co-mutations *KEAP1* and *STK11/Lkb1* on the metabolic and immune microenvironment of lung adenocarcinoma in immune-intact models, we generated a cohort of GEMMs to reflect the diverse tumor suppressor land-

scape seen in patients. Mice carrying the *Kras*^{G12D/+} allele (K) (Jackson et al., 2001) were crossed with *Keap1*^{fllox/fllox} (KK) (Blake et al., 2010) and/or *Lkb1*^{fllox/fllox} (KKL, KL) (Bardeesy et al., 2002) mice and genetic recombination induced by intranasal inhalation of Ad5-CMV-Cre adenovirus (Best et al., 2018b). Loss of *Lkb1*, alone or in combination with *Keap1*, significantly reduced the latency in the *Kras*^{G12D} cohort (KK 71 days [Best et al., 2019], KL 48 days, and KKL 49 days), suggesting a dominating role of *Lkb1* in *Kras* tumorigenesis (Figure 1A). Both *Keap1* and *Lkb1* proteins are upstream of key metabolic pathways in the cell; hence, to dissect differential tumor-associated metabolites, we performed steady-state metabolomics on pieces of tumor tissue. Supporting our ability to detect differential metabolites from tumors independent of their anatomical location, no region-specific differences were found in normal or tumor-bearing lungs, with the strongest differences arising between normal and lung tumors (Figures S1A–S1C). We interrogated the metabolites present in tumor nodules collected from cohorts of KK, KL, and KKL mice. Strikingly, the tumor metabolites from each genotype were distinct and clustered separately by principle component analysis (Figure 1B). Indeed, metabolites detected in the *Lkb1*-deficient tumors were significantly distinct from those detected in KK tumors, measured by Euclidean hierarchical clustering (Figures 1C and S1D). Direct comparison of KL compared with KK tumors revealed many differentially abundant metabolites, associated with well-established *Lkb1*- and *Keap1*-related metabolic pathways (Figures 2A and 2B). In KK tumors, the pentose phosphate pathway (PPP) is strongly regulated by NRF2 activity (Best et al., 2018a, 2019). The steady-state analysis identified a branchpoint in PPP metabolite abundance at the enzyme *phosphoribosyl pyrophosphate amidotransferase* (PPAT), resulting in reduced abundance of the upstream metabolite sedoheptulose-7P in KK tumors, whereas metabolites downstream exhibited significantly increased abundance (Ribose or inosinic acid [IMP]) (Figure 2C). GSH, which is strongly regulated by the NRF2 pathway (Best et al., 2018a, 2019; Mitsuishi et al., 2012; Singh et al., 2013), was similarly increased in KK tumor nodules (Figures 2D and S1E). The lack of enrichment of signature NRF2 pathway metabolites in KKL tumor nodules suggests that metabolic rewiring induced by *Lkb1*-loss, likely via the AMPK and SIK pathways (Pierce et al., 2021), dominate that of NRF2 pathway activation. The lack of abundant GSH in KKL tumors suggests that Gln, shuttled by NRF2-active tumors via xCT to increase intracellular cystine for GSH production (Romero et al., 2017; Sayin et al., 2017), may be utilized in alternative pathways in tumors that are also *Lkb1* deficient. Indeed, levels of GSH were similar between KL and KKL tumor nodules in an independent steady-state metabolomics cohort (Figure S1F). Comparing KL and KK tumor metabolites revealed that Glu-related pathways are significantly altered between the two tumors (Figure 2E). In line with our hypothesis, relatively similar quantities of Gln between the KK and KL tumor nodules resulted in significantly enhanced Glu production in *Lkb1*-deficient tumors (Figure 2F). To further investigate this finding across the spectrum of *Kras*^{G12D} co-mutant models (Skoulidis et al., 2015), we compared the steady-state metabolomics between K, *Kras*^{G12D/+};p53^{ΔΔ} (KP), KK, KL, and KKL tumor nodules. Distinctly, KL was the only tumor model that displayed significantly elevated Glu in the tumor nodules (Figures 2G and S1G).

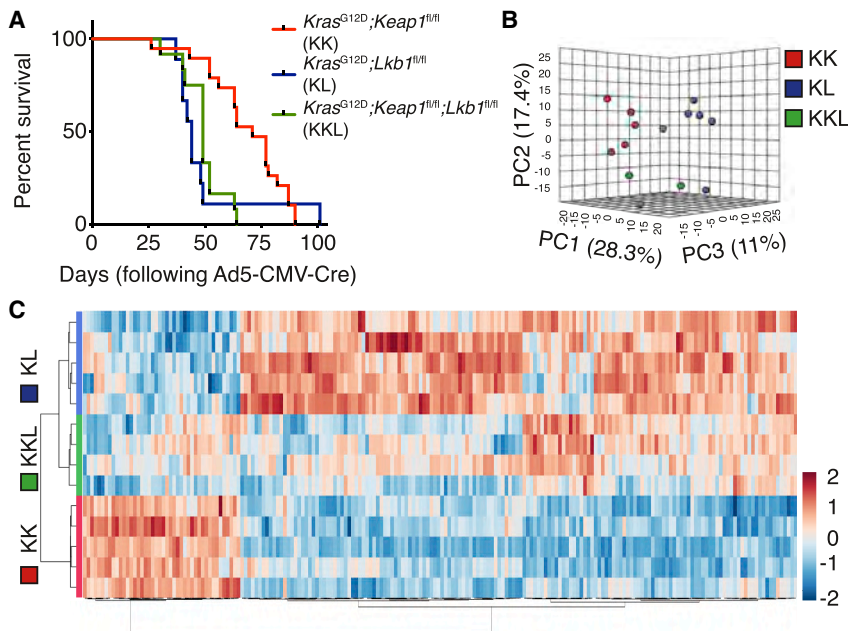


Figure 1. Loss of *Lkb1* accelerates *Kras*^{G12D/+};*Keap1*^{Δ/Δ} tumorigenesis

(A) Survival analysis of *Kras*^{G12D/+};*Keap1*^{Δ/Δ} (KK; n = 19), *Kras*^{G12D/+};*Lkb1*^{Δ/Δ} (KL; n = 9) and *Kras*^{G12D/+};*Keap1*^{Δ/Δ};*Lkb1*^{Δ/Δ} (KKL; n = 12) mice (Mantel-Cox test $p < 0.0001$).

(B) Principle component (PC) analysis comparing the steady-state metabolome of *Kras*^{G12D/+};*Keap1*^{Δ/Δ} (KK; n = 5), *Kras*^{G12D/+};*Lkb1*^{Δ/Δ} (KL; n = 5) and *Kras*^{G12D/+};*Keap1*^{Δ/Δ};*Lkb1*^{Δ/Δ} (KKL; n = 4) tumors.

(C) Top 200 differentially abundant metabolites in KK (n = 5), KL (n = 5) and KKL (n = 4) tumor nodules.

This suggests that there may be a specific dependence for Glu in *Lkb1*-deficient *Kras*^{G12D} tumors.

Increased glutamate production in *Lkb1*-deficient tumors

Next, we sought to examine glutaminase activity in tumor cells themselves. NRF2 pathway activation leads to increased expression of SLC1A5, resulting in an association of *KEAP1* mutations with enhanced *GLS1* expression and glutaminase activity (Romero et al., 2017; Sayin et al., 2017). In the GEMMs, *Gls1* exhibited high mRNA expression in the KL tumor nodules, suggesting a strong association with *Lkb1* loss alone (Figure 3A). Stratification of *GLS1* mRNA expression in *KRAS*-mutant lung adenocarcinoma patient samples (Figure 3B) or cell lines (Figure 3C) similarly identified a stronger correlation with mutations in *STK11/Lkb1*. To investigate the activity of glutaminase and usage of Glu in the *Lkb1*-deficient TME, we performed labeled U-¹³C₅,U-¹⁵N-Gln tracing assays in tumor-bearing KL and KKL mice. Glutaminase activity can be measured by comparing labeled ¹³C₅,¹⁵N₂ Gln and ¹³C₅,¹⁵N₁ Glu. Glu can be exported for cystine via xCT or converted to α -ketoglutarate (α -KG) for energy production (Figure S2A). The use of α -KG in the cell can be detected by labeled aspartate (Asp), whereby α -KG is shuttled into the citric acid cycle (CAC) and generates ¹³C₄,¹⁵N₁ Asp, although under hypoxic conditions, ¹³C₃,¹⁵N₁ Asp is generated from α -KG via the reductive pathway (Wang et al., 2019; Figure 3D). To measure the *in vivo* utilization of Gln, we performed a 15-min pulse of U-¹³C₅,U-¹⁵N-Gln, sufficient to label 60%–70% of the Gln in normal lung, KL tumor tissue, and KKL tumor tissue (Figure 3E). Unlike the normal lung, *Lkb1*-deficient tumors had a significant increase in Gln conversion to Glu (both ¹³C₅ and ¹³C₅,¹⁵N₁), suggesting increased glutaminase activity in tumor cells during the 15-min pulse (Figure 3F). Interestingly, Gln nitrogen can be used to generate IMP, independent of glutaminase (Figure S2B). Levels of ¹⁵N₂ IMP were increased in KKL tumor nodules compared with KL (Figure S2C),

suggesting that increased glutaminase activity in KL tumors results in more Glu to Glu hydrolysis. Furthermore, significant flux through the CAC was detected in *Lkb1*-deficient tumors through the generation of Asp (both ¹³C₄ and ¹³C₄,¹⁵N₁) and the emergence of ¹³C₃,¹⁵N₁ Asp, reflective of a hypoxic tumor environment (Wang et al., 2019), which was more pronounced in KL tumor nodules (Figure 3G). Thus, Gln is rapidly utilized in *Lkb1*-deficient tumors to produce Glu to feed the CAC (Figure S2A).

Recently, the pool of orotate in the tumor and circulating plasma has been described as a nitrogen sink from the hypoxic tumor environment and increased usage of Gln (Wang et al., 2019). To further investigate this, we generated an independent steady-state metabolomics cohort, in which we analyzed both the tumor nodules or lung and the plasma from normal (UN), KL, and KKL mice. We identified significantly elevated orotate in the tumor nodules compared with normal lung samples, indicative of a hypoxic TME (Figure S2D). Concordant with increased abundance of Asp at steady state (Figure S2E) and ¹³C₃,¹⁵N₁ Asp in KL tumor nodules (Figure 3G), orotate was further increased in KL compared with KKL and KK (Figure S2F). Gln nitrogens were confirmed to be the source of increased orotate via the urea cycle (Kim et al., 2017; Figure S2G). Consistent with our analysis of tumor nodules, we identified significantly increased orotate levels in the circulating plasma of the tumor-bearing KL and KKL mice, 40 days post tumor initiation (Figure S2H). Together with previous reports (Wang et al., 2019), these data suggest that the emergence of orotate in the plasma may be indicative of a pan-cancer oncometabolite and worthy of further investigation.

Glutamate availability impacts CD8 T cell activation

During activation, T cells switch from catabolic to anabolic metabolism, and metabolite availability, especially that of glucose and Gln, is essential for resting T cells to become activated (Pearce et al., 2013; Sinclair et al., 2013). To investigate immune cell infiltration and activation in a TME with different Gln availability, we performed immune analysis on tumor-bearing lungs collected at defined time points. Although *KEAP1*- and *STK11/Lkb1*-mutant tumors are considered immune cold, the relative abundance of immune cells was increased in *Lkb1*-deficient (KL and KKL) tumor-bearing lungs, relative to KK, with evidence of immune

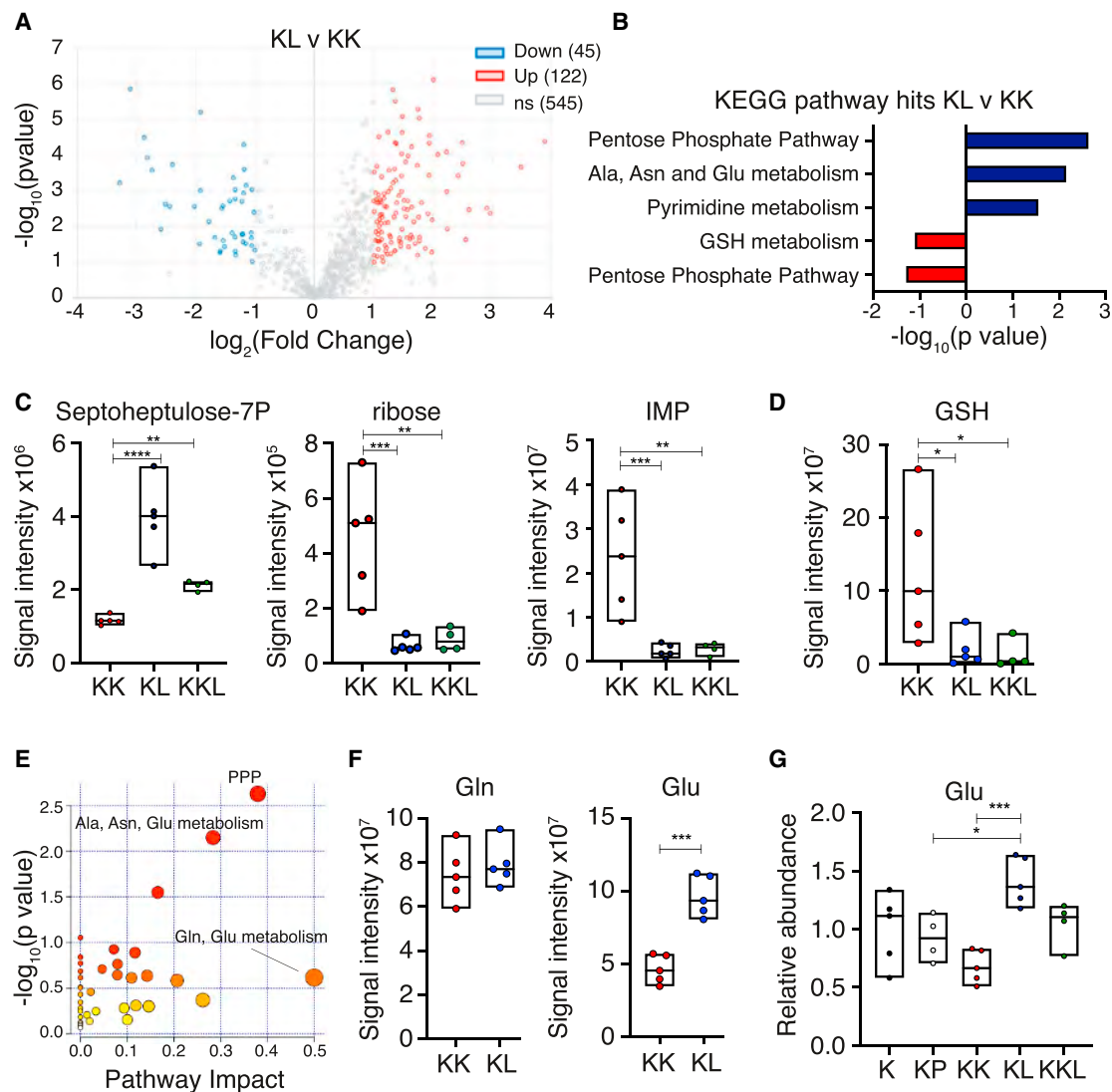


Figure 2. Co-mutation in *Kras*^{G12D/+} lung adenocarcinoma alters the metabolome of tumors

(A) Volcano plot of KL compared with KK metabolites. Red metabolites are significantly increased in abundance, and blue are significantly reduced. ns, not significant.

(B) KEGG pathways associated with significantly altered metabolites in KL versus KK tumors (blue: up in KL; red: up in KK).

(C) Abundance of sedoheptulose-7-phosphate, ribose and inosinic acid (IMP) in KK (n = 5), KL (n = 5) and KKL (n = 4) tumors. Ordinary one-way ANOVA S7P: KK versus KL: p < 0.0001; KL versus KKL: p = 0.0019; ribose: KK versus KL: p = 0.0014; KK versus KKL: p = 0.0032; IMP: KK versus KL p = 0.0026; KK versus KKL: p = 0.0047.

(D) Abundance of glutathione (GSH) in KK (n = 5), KL (n = 5), and KKL (n = 4) tumors. Ordinary one-way ANOVA KK versus KL: p = 0.0454; KK versus KKL: p = 0.0455.

(E) Metabolic pathway impact plot measuring the significance ($-\log_{10}$ (p value)) and impact (proportion of pathway altered).

(F) Abundance of glutamine (Gln) and glutamate (Glu) in KK (n = 5) and KL (n = 5) tumors. Ordinary one-way ANOVA Glu KK versus KL p = 0.0001.

(G) Relative abundance of glutamate (Glu) in K (n = 5), KP (n = 4), KK (n = 5), KL (n = 5), and KKL (n = 4) tumor nodules. Ordinary one-way ANOVA KP versus KL p = 0.0258; KK versus KL p = 0.0004.

engagement (Figures 4A, 4B, S3A, and S3B). Consistent with previous reports, *Lkb1*-deficient models displayed a mixture of squamous and adenomatous lesions; hence, the cohort was divided to investigate immune features independently (Figure S3C). In line with prior reports (Koyama et al., 2016), we identified increased proportions of neutrophils in *Lkb1*-deficient models with a mixture of adeno and squamous (A/S mix) features (Figure 4C). Furthermore, an increased regulatory T cell (Treg;

identified by FoxP3) to CD8 T cell ratio in the tumor-bearing lungs of KKL mice (Figure S3D) revealed a significant increase in T regs, especially in tertiary lymphoid structures (TLSs) (Figures S3E and S3F). To validate these findings, we performed RNA sequencing (RNA-seq) on tumor nodules from each of the models (KK, KL, and KKL) and uninfected (UN) littermate controls. We confirmed the significant increase in *FoxP3* transcript in KKL tumors, strongly suggesting a significant relationship of

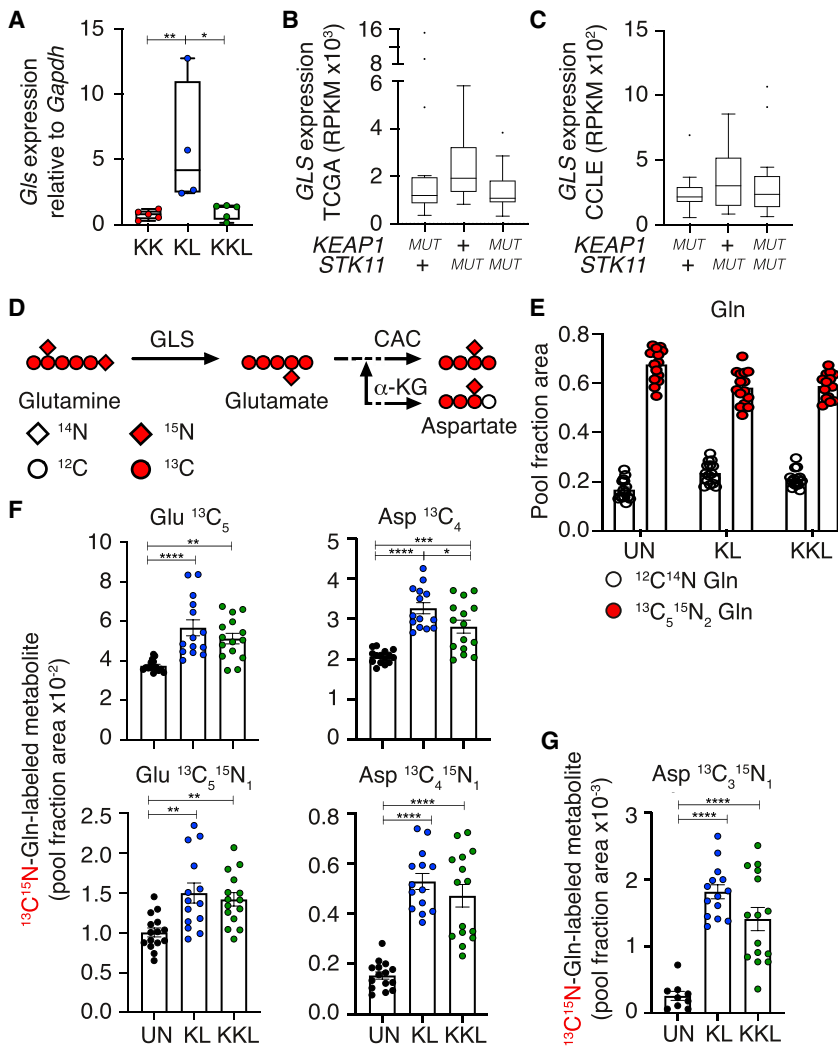


Figure 3. Increased glutamine flux in *Lkb1*-deficient lung tumor nodules

(A) *Gls* mRNA expression in KK (n = 5), KL (n = 4), and KKL (n = 5) tumor nodules.

(B) Expression of glutaminase (*GLS1*) in *KRAS*-mutant lung adenocarcinoma from the TCGA cohort (n = 102) co-mutated with *KEAP1* (n = 16) and/or *STK11* (n = 21; 16).

(C) Expression of *GLS1* in *KRAS*-mutant lung adenocarcinoma (n = 139) co-mutated with *KEAP1* (n = 16) and/or *STK11* (n = 16, 19) from the CCLE dataset.

(D) Schematic of $^{13}\text{C}_5^{15}\text{N}_2$ -glutamine (Gln) flux to glutamate (Glu) through to aspartate (Asp) via the citric acid cycle (CAC) or α -ketoglutarate (α -KG) intermediates.

(E) Fraction of unlabeled ($^{12}\text{C}^{14}\text{N}$ -Gln) and labeled ($^{13}\text{C}_5^{15}\text{N}_2$ -Gln) glutamine in normal (UN; n = 5; 4 tissue pieces/lung) compared with KL (n = 5; 4 tumor pieces/lung) and KKL (n = 5; 4 tumor pieces/lung) lung.

(F) Fraction of $^{13}\text{C}_5^{15}\text{N}$ -Gln label in $^{13}\text{C}_5$ - and $^{13}\text{C}_5^{15}\text{N}_1$ -Glu, $^{13}\text{C}_4$ -, $^{13}\text{C}_4^{15}\text{N}_1$ - in tumor nodules. Ordinary one-way ANOVA $^{13}\text{C}_5$ -Glu UN versus KL p < 0.0001; UN versus KKL p = 0.0026; $^{13}\text{C}_5^{15}\text{N}_1$ -Glu UN versus KL p = 0.0013; UN versus KKL p = 0.0063; $^{13}\text{C}_4$ -Asp UN versus KL p < 0.0001; UN versus KKL p = 0.0003; KL versus KKL p = 0.03; $^{13}\text{C}_4^{15}\text{N}_1$ -Asp UN versus KL p < 0.0001; UN versus KKL p < 0.0001.

(G) Fraction of $^{13}\text{C}^{15}\text{N}$ -Gln label in $^{13}\text{C}_3^{15}\text{N}_1$ -Asp in tumor nodules. Ordinary one-way ANOVA $^{13}\text{C}_3^{15}\text{N}_1$ -Asp UN versus KL p < 0.0001; and UN versus KKL p < 0.0001.

Tregs with these tumors (Figure S3G). To infer the impact of increased Glu on the activity of CD8 T cells in the tumors of KL mice, we next assessed cytotoxic gene signatures in the tumor nodules. We identified increased granzyme and interferon (IFN) genes in KL tumors compared with the other tumor models (Figures 4D and S3H), suggesting that there may be increased activation of CD8 T cells in the high Glu TME.

We next wished to directly examine the role of Glu for CD8 T cell activation. Gln is transported into the cell by SLC1A5 and hydrolyzed to Glu by the enzymatic activity of *Gls1* (Pearce et al., 2013; Wang et al., 2010). To directly assess the role of glutaminase activity in CD8 T cell activation, we investigated a glutaminase conditional knockout mouse model (Johnson et al., 2018). Acute infection of mice with lymphocytic choriomeningitis virus (LCMV) Armstrong drives TCR-mediated expansion of CD8 T cells. We adoptively transferred equal numbers of glutaminase-deficient (*Gls1*^{fl/fl}; *CD4Cre*) or control (*Gls1*^{+/+}; *CD4Cre*) P14 CD8 TCR transgenic T cells, which are specific for the LCMV-derived gp33-41 epitope, into congenically marked (Ly5.1) recipient mice. Recipient mice were infected with LCMV, and the expansion of donor P14 cells was measured

on days 6 and 13 postinfection (Figure 4E). Consistent with the importance of Gln and glutaminase activities in CD8 T cells, *Gls1*-deficient CD8 T cells failed to expand as efficiently as control P14 cells (Figure 4F). Thus, increased abundance of Glu in the KL TME could correlate with the capacity of CD8 T cells to be activated, and *Gls1* is required for efficient population expansion of antigen specific CD8 T cells in response to TCR stimulation.

CD8 T cell clonotype expansion is hindered by glutaminase inhibition

Enhanced Glu abundance and usage by KL tumors is likely to impact the metabolic activity of CD8 T cells present in the TME. Recently, Gln antagonism (Leone et al., 2019) and glutaminase inhibition (Johnson et al., 2018) have been shown to enhance the cytotoxic effector function of CD8 T cells. Given the poor response of patients with *KRAS/STK11*-mutant lung adenocarcinoma to immunotherapy (Papillon-Cavanagh et al., 2020; Singh et al., 2021), we reasoned that KL mice would be a strong immunocompetent model to test the hypothesis that glutaminase inhibition (CB-839) could synergize with immunotherapy (anti-PD1) to enhance the antitumor CD8 T cell response. To this end, we performed a short-term drug study to measure the response of CD8 T cells in the TME to glutaminase inhibition and anti-PD1 immunotherapy (Figure 5A). Dosing schedules were consistent with

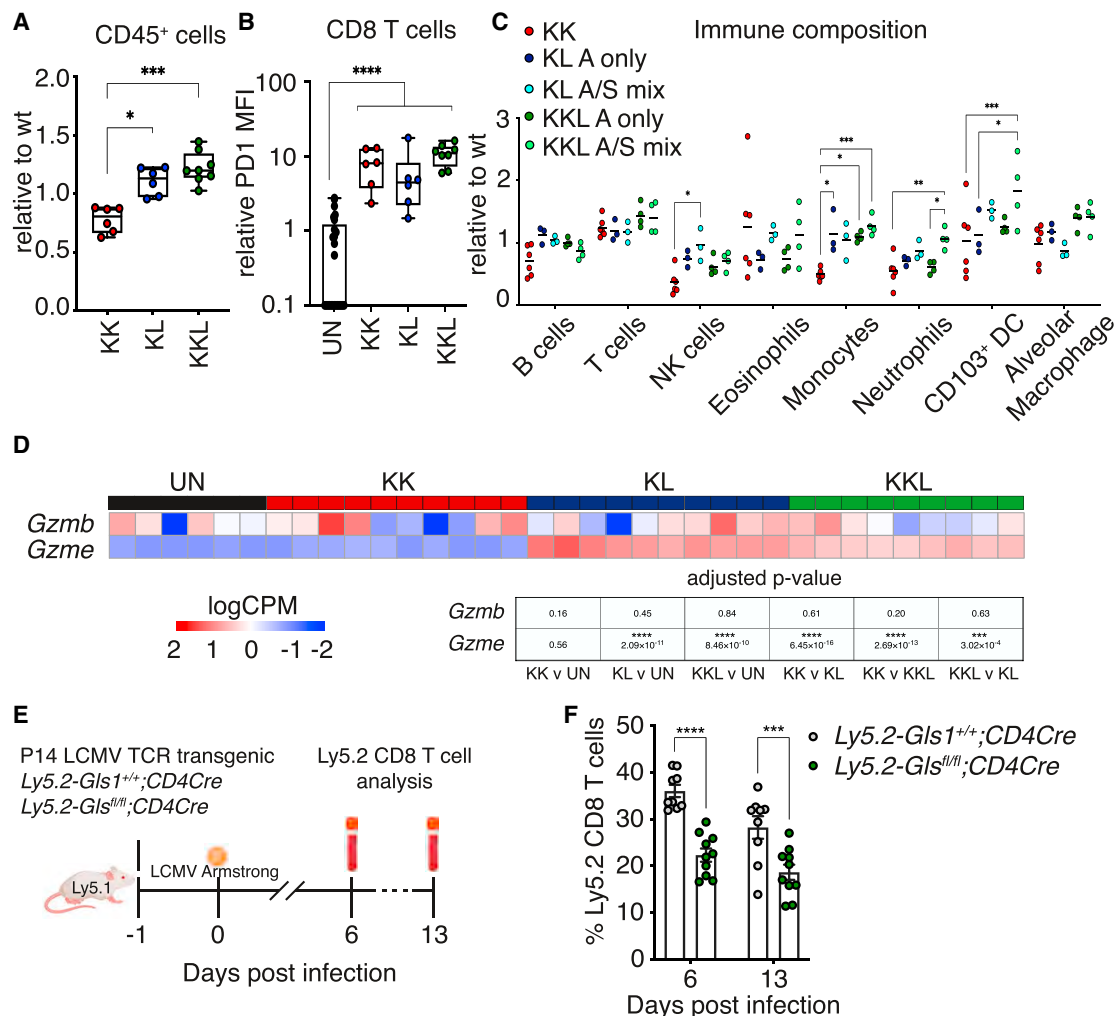


Figure 4. Increased glutamate alters the immune activity in the *Kras*^{G12D/+};*Lkb1*^{Δ/Δ} (KL) tumor microenvironment

(A) Quantification of CD45⁺ immune cells in the tumor-bearing lungs of KK (n = 6), KL (n = 8) and KKL (n = 8) mice. Ordinary one-way ANOVA KK versus KL p = 0.015; KK versus KKL p = 0.0005.

(B) Flow cytometry quantification of PD1 expression on CD8 T cells in the lungs of WT (n = 25) and KK (n = 6), KL (n = 6), and KKL (n = 8) tumor-bearing lungs. Ordinary one-way ANOVA p < 0.0001.

(C) Quantification of B cells (CD45⁺CD19⁺), T cells (CD45⁺CD3⁺), NK cells (CD45⁺NKp46⁺DX5⁺), eosinophils (CD45⁺CD11b⁺Ly6G⁻SSC^{high}), monocytes (CD45⁺CD11b⁺Ly6G⁻SSC^{low}), neutrophils (CD45⁺CD11b⁺Ly6G⁺), CD103⁺DC (CD45⁺CD11c⁺CD103⁺) in KK (n = 6), KL A only (n = 3), KL A/S mix (n = 3), KKL A only (n = 4), and KKL A/S mix (n = 4) tumor-bearing lungs. Two-way ANOVA with Tukey's multiple comparisons test: NK cells KK versus KL A/S p = 0.04; monocytes KK versus KL A p = 0.018, KK versus KKL A p = 0.016, and KK versus KKL A/S p = 0.0007; neutrophils KK versus KKL A/S p = 0.0019, KKL A versus KKL A/S p = 0.011; CD103⁺DC KK versus KKL A/S p = 0.0004; and KL A versus KKL A/S p = 0.017.

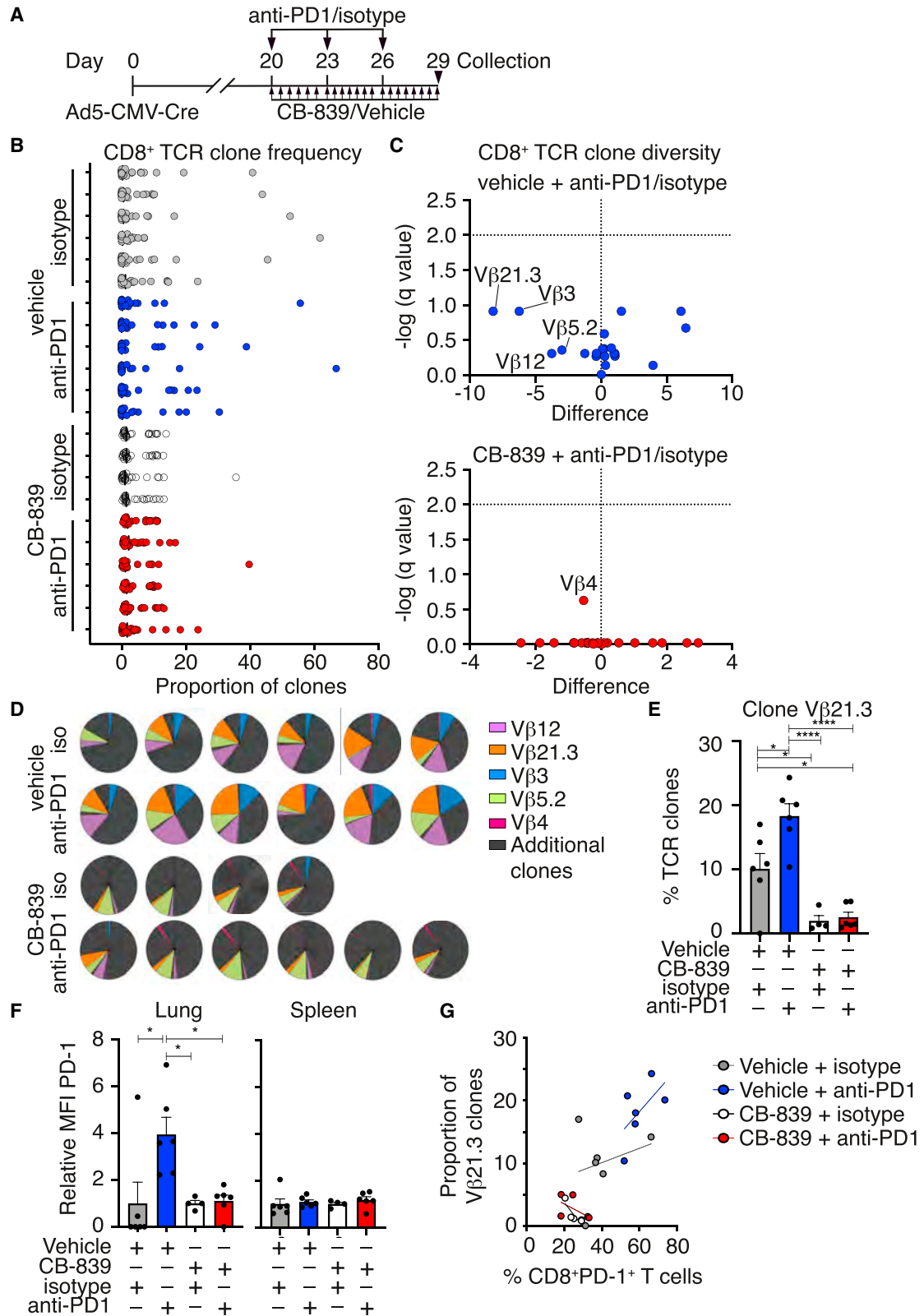
(D) Heatmap representing the logCPM transcript of *Gzmb* and *Gzme* in uninfected (UN; n = 6) and tumor nodules (2 per lung) in KK (n = 5), KL (n = 5), and KKL (n = 5) mice. Adjusted p value of pairwise comparisons are displayed.

(E) Schematic of LCMV infection protocol. Briefly, Ly5.1 recipient mice received Ly5.2 P14 LCMV TCR transgenic cells 1 day prior to LCMV Armstrong infection. Following 6 and 13 days postinfection, blood was analyzed for the proportion of Ly5.2 CD8 T cells by flow cytometry.

(F) Quantification of Ly5.2 P14 CD8 T cells from *Gls1*^{+/+};*CD4Cre* (n = 9) and *Gls1*^{fl/fl};*CD4Cre* (n = 10) donors at 6 and 13 days postinfection. Two-way ANOVA day 6 p < 0.0001; day 13 p = 0.0008.

previous tumor studies, with CB-839 administered twice daily (200 mg/kg) (Galan-Cobo et al., 2019; Romero et al., 2017) and anti-PD1 every third day (Best et al., 2018a). As expected with this short treatment schedule, there was no change in overall tumor burden, measured by lung weight (Figure S4A). We additionally did not identify any gross alterations in the abundance of immune cells (CD45) or T cells (CD3) in the tumor-bearing lungs of any of the treatment arms (Figures S4B and S4C).

Clonotype frequency is a robust indicator of antigen recognition and CD8 T cell expansion in the TME (Corgnac et al., 2020). We measured the abundance of 24 Vβ TCR clonotypes in CD8 T cells using flow cytometry and identified a significant clonotype expansion in the tumor-bearing lungs of KL mice treated with anti-PD1 alone (Figure 5B). This expansion was local to the lung and not apparent in the circulation, as measured in splenic CD8 T cells (Figure S4D). Critically, KL mice that received



(legend on next page)

CB-839 displayed minimal clonotype expansion with or without anti-PD1 (Figure 5B), suggesting that glutaminase inhibition blocked activation-induced CD8 T cell expansion. To measure the V β clonotypes that were expanding in anti-PD1-treated cohorts, we plotted the variance in the vehicle or CB-839 groups comparing isotype with anti-PD1 treatment. Although many clonotypes were significantly altered by anti-PD1 treatment in vehicle-treated mice, a reduced variance was observed in mice treated with CB-839 (Figure 5C). Next, clonotype diversity was compared between individual mice (Figure 5D). Consistent with clonal expansion, anti-PD1 significantly increased the proportions of V β 21.3, 12, and 3 in each mouse compared with isotype control in the absence of glutaminase inhibition. Comparatively, no clonotypes were significantly altered across the mice in the CB-839 cohorts, confirming the broader cohort analysis. As a specific example, TCR clonotype V β 21.3 is significantly increased in the tumor environment of anti-PD1-treated mice, but not in mice treated with CB-839, with or without anti-PD1 (Figures 5E and S4E). In line with these observations, we identified increased PD1 expression on CD8 T cells in the tumor environment of the lungs and not spleen (Figure 5F) and increased type 1 conventional dendritic cells (cDC1) in the lungs of anti-PD1-treated mice (Figure S4F). Increased V β 21.3 clonotype expansion was relative to the proportion of CD8⁺PD1⁺ T cells, only in anti-PD1-treated mice (Figure 5G), further suggesting that glutaminase inhibition impaired the activation and clonotype expansion of CD8 T cells in the TME. Consistent with patient studies, anti-PD1 had no survival benefit in KL mice and induced a robust expansion in effector T regulatory cells during tumor progression (Figures S4G and S4H).

Reduced effector CD8 T cells in the lungs of glutaminase-inhibitor-treated mice

To investigate the impact of glutaminase inhibition on T cell differentiation in the TME, we analyzed the unbiased clustering of CD8 T cells by tSNE based on the expression of four key T cell markers (CD44, CD62L, PD1, and TCF1) assessed by flow cytometry. We identified 7 distinct clusters (Figure S5A). To distinguish clusters that represent CD8 T cells activated in response to lung tumors, we overlaid the CD8 T cells from non-tumor-bearing lungs of C57BL/6 mice (Figure S5B). In comparison to C57BL/6 mice, cluster 1 was enriched specifically in tumor-bearing mice. Consistent with this notion, cluster 1 cells expressed the highest levels of CD44, indicative of tumor recognition (Figure S5C). Next, we assessed the relative contributions of each treatment arm to

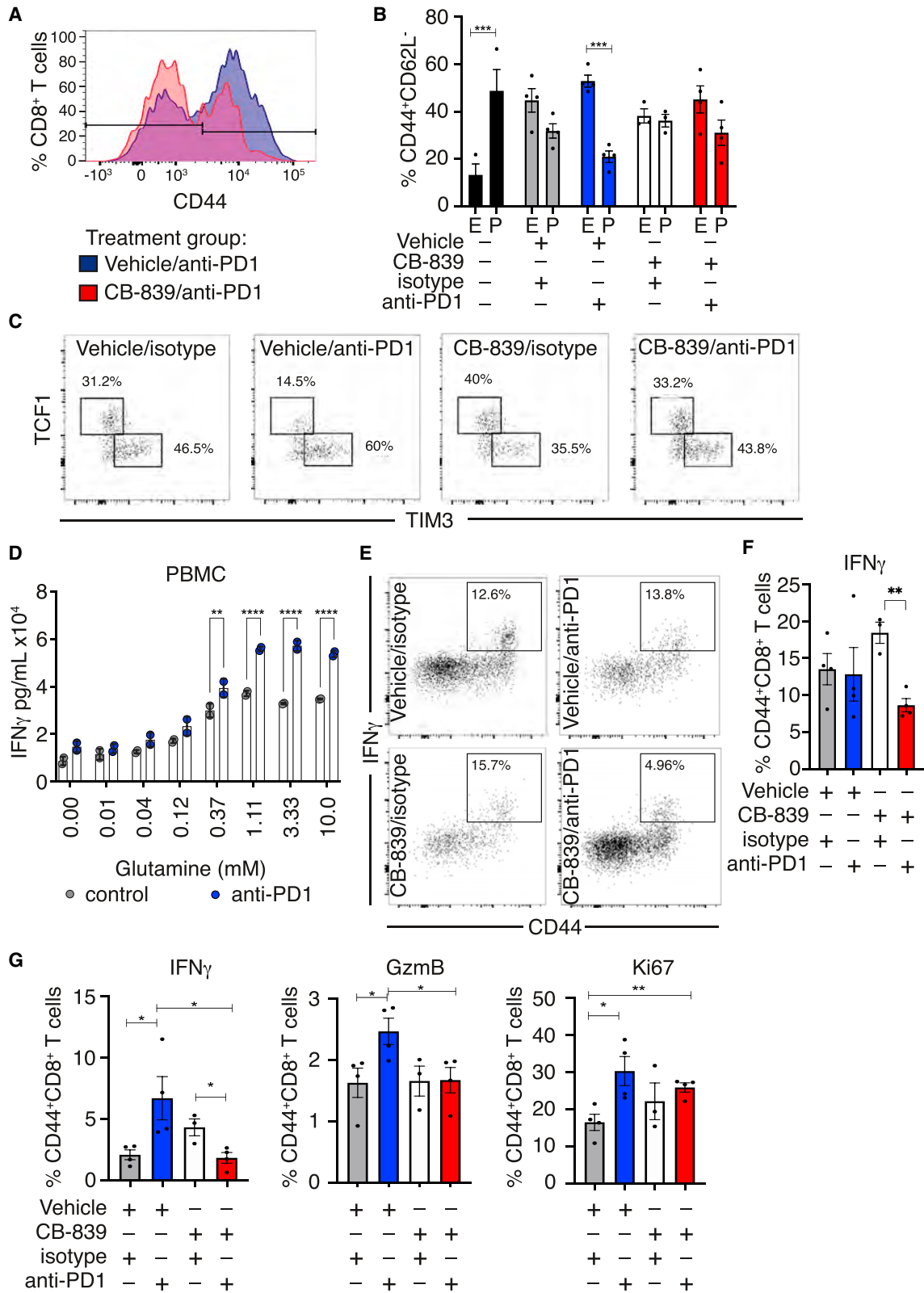
the highly active cluster 1, which was enriched in vehicle-/anti-PD1-treated CD8 T cells (Figure S5D). Consistent with the unbiased cluster approach, the effector CD44⁺ population was increased in CD8 T cells from tumors of vehicle-/anti-PD1-treated mice, compared with those treated with CB-839 with anti-PD1 (Figure 6A), suggesting that glutaminase inhibition impeded the expansion of effector CD8 T cells. Strikingly, this activation was only present in the TME, whereby increased CD44⁺PD1⁺ CD8 T cells were observed in the tumor-bearing lungs (Figure S5E) but not in splenic T cells (Figure S5F). Although activation of CD8 T cells is minimal beyond the tumor-bearing lungs, CB-839 significantly reduced the proportion of CD8⁺CD44⁺ effector T cells observed in the spleen (Figure S5G), highlighting the systemic effects of glutaminase inhibition on CD8 T cells. To investigate in depth the phenotypic differentiation of CD8 effector T cells, we interrogated the expression of the transcription factor TCF1. CD8 T cells expressing TCF1 represent a progenitor pool that continuously populates the effector/exhausted T cells and is responsible for mediating response to PD1 checkpoint inhibition (Im et al., 2016; Utzschneider et al., 2016; Kallies et al., 2020). Thus, the effector T cell can be identified as TCF1⁺TIM3⁺ (Utzschneider et al., 2020) and arises from the TCF1⁺ pool (Kallies et al., 2020). In the lungs of C57BL/6 non-tumor-bearing mice, TCF1⁺ CD8 T cells were significantly more abundant (48% \pm 8.5%) than the TCF1⁻ cells (13% \pm 3.9%), indicative of the absence of TCR stimulation (Figures 6B and S6A). Notably, the TCF1⁻ effector pool expanded significantly in the tumor-bearing lungs of anti-PD1-treated mice (52% \pm 1.5%) but was impaired in mice that received the combination with CB-839 (45% \pm 4.7%) (Figures 6B and 6C). These altered ratios were not observed in the periphery (Figure S6B). These results suggest that anti-PD1-mediated expansion of effector CD8 T cells requires efficient glutaminase metabolism.

Activated CD8 T cells require glutaminase activity to sustain an antitumor state

It has previously been found that naïve CD8 T cells respond robustly to TCR stimulation even in the presence of glutaminase inhibition (Johnson et al., 2018). However, as Gln is essential to sustain the bioenergetic needs of activated T cells, we hypothesized that the combination of TCR stimulation and anti-PD1 immunotherapy enhanced the requirement of CD8 T cells for glutaminase activity. To test this theory in a patient model *in vitro*, we stimulated human peripheral blood mononuclear cell (PBMC)-derived T cells in different concentrations of Gln

Figure 5. CD8 T cell clonal expansion is hindered by glutaminase inhibition

- (A) Schematic of drug treatment study. Briefly, KL mice were intranasally injected with Ad5-CMV-Cre to induce genetic recombination. From day 20, mice were treated twice daily with glutaminase inhibitor CB-839 or vehicle, with anti-PD1 or isotype. Lungs and spleens were collected on day 29 for flow cytometry of TCR V β chain clonality analysis of CD8 T cells.
- (B) Lung infiltrating CD8 T cell TCR clonal analysis in KL mice (vehicle/isotype n = 6; vehicle/anti-PD1 n = 6; CB-839/isotype n = 4; CB-839/anti-PD1 n = 6).
- (C) Frequency of significantly different TCR V β clones in vehicle- and CB-839-treated mice. Noted TCR clones were increased in anti-PD1 treated mice compared with isotype.
- (D) Frequency of TCR V β clones in lung infiltrating CD8 T cells. Each wheel represents the clonal diversity of one mouse.
- (E) Frequency of TCR clone V β 21.3 in lung infiltrating CD8 T cells. Ordinary one-way ANOVA V iso versus PD1 p = 0.014; V iso versus CB-839 iso p = 0.032; V iso versus CB-839 PD1 p = 0.025; V PD1 versus CB-839 iso p < 0.0001; and V PD1 versus CB-839 PD1 p < 0.0001.
- (F) Expressions of PD1 on CD8 T cells in the lung (left) and spleen (right). Ordinary one-way ANOVA V iso versus PD1 p = 0.018; V PD1 versus CB-839 iso p = 0.038; and V PD1 versus CB-839 PD1 p = 0.024.
- (G) Proportion of CD8⁺PD1⁺ T cells relative to the frequency of V β 21.3 in lung infiltrating CD8 T cells in vehicle/isotype (n = 6); vehicle/anti-PD1 (n = 6); CB-839/isotype (n = 4); and CB-839/anti-PD1 (n = 6).



(legend on next page)

with and without anti-PD1 stimulation and measured interferon gamma (IFN γ) production by ELISA assay (Figure S6C). As expected, both increasing availability of Gln and anti-PD1 stimulation resulted in enhanced IFN γ production. However, the benefit of anti-PD1 stimulation was only achieved when Gln concentrations increased above 0.37 mM (Figure 6D). To confirm these findings *in vivo*, we took splenic CD8 T cells from mice treated with anti-PD1 and/or CB-839 and stimulated *ex vivo* for 6 h with phorbol myristate acetate (PMA) and ionomycin and quantified the production of IFN γ in effector (CD44⁺) CD8 T cells by flow cytometry (Figure 6E). Although CB-839 alone resulted in a slight increase in IFN γ production following stimulation, the combination with anti-PD1 resulted in a significant reduction in IFN γ production (Figure 6F) and proliferation as measured by Ki67 expression (Figure S6D). This suggests that the stimulation benefit afforded by anti-PD1 comes at a cost of increased Gln consumption, thus necessitating the enzymatic activity of glutaminase.

Next, to assess the functional consequences of glutaminase inhibition with anti-PD1 in the TME, production of cytotoxic IFN γ and granzyme B (GzmB) from CD8 T cells was examined in the tumor-bearing lungs of KL mice. Following treatment with anti-PD1 and/or CB-839, tumor-bearing lungs were harvested and CD8 T cells were stimulated *ex vivo* for 6 h with PMA and ionomycin. Consistent with our exploratory experiments, we identified a significant reduction in IFN γ , GzmB, and proliferation in CD8 T cells pretreated with the combination of anti-PD1 and CB-839 (Figures 6G and S6E–S6G). Notably, minor gains in IFN γ production afforded by CB-839 monotherapy were abolished in combination with anti-PD1. Taken together, these data strongly suggests that immunotherapy increases the dependency of CD8 T cells on Gln availability and glutaminase enzymatic activity, resulting in a loss of therapeutic benefit when anti-PD1 and CB-839 are combined.

DISCUSSION

The heterogeneity imbued by co-mutation within *KRAS*-mutant lung adenocarcinoma is an emerging field of interest (Best et al., 2019; Papillon-Cavanagh et al., 2020; Skoulidis et al., 2015; Skoulidis and Heymach, 2019). Not only are *TP53*, *KEAP1*, and *STK11/Lkb1* potent tumor suppressors in the context of *KRAS*-mutant lung adenocarcinoma (Best et al., 2019; Jackson et al., 2005; Ji et al., 2007), but each impart distinct phenotypic characteristics that have the potential to

leverage therapeutic design (Best et al., 2019) or act as biomarkers of impaired therapeutic response (Papillon-Cavanagh et al., 2020; Singh et al., 2021). Indeed, mutation in *STK11* is a genomic correlate of poor PD-L1 expression (Lamberti et al., 2020) and anti-PD-L1 (atezolizumab) response (Ricciuti et al., 2022; Singh et al., 2021) in NSCLC. Improving the response of *STK11*-mutant lung adenocarcinoma to immunotherapy is an emerging challenge. Here, we find that the *Lkb1*-deficient TME is rich in Glu, an essential nutrient for CD8 T cell activation and cytotoxicity. Although this environment provides good rationale for treatment with glutaminase inhibition and immunotherapy, our findings do not support the combination due to critical impairment of CD8 T cell effector function.

It is recently increasingly appreciated that *KRAS*-mutant lung adenocarcinomas represent a spectrum of diseases dictated by the properties of concurrent mutations in critical tumor suppressors (Best et al., 2019; Kerk et al., 2021; Papillon-Cavanagh et al., 2020; Skoulidis et al., 2015; Skoulidis and Heymach, 2019). Here, we further establish that the metabolic environment of *Kras*-mutant tumors is significantly altered based on combinatorial inactivation of *Keap1* or *Lkb1*. This highlights the importance of annotating the concurrent mutations in key tumor suppressors within *KRAS*-mutant lung adenocarcinoma to fully comprehend the characteristics of the tumor. For example, a recent study confirmed that *KEAP1* mutations are a negative prognostic factor for advanced stage NSCLC (Saleh et al., 2022), although both *STK11* and *KEAP1* mutations confer poor outcomes to immunotherapy in *KRAS*-mutant, but not in *KRAS* wild-type cancers (Ricciuti et al., 2022). Furthermore, metabolic changes associated with inactivation of *Lkb1* were dominant over those of *Keap1*, with KKL tumors displaying metabolic properties similar to KL tumors. This has a significant impact on the study of *KEAP1*-mutant lung adenocarcinoma, where the majority of cell lines and patient samples harbor co-mutations of *STK11/Lkb1*. Importantly, *Lkb1*-deficient tumors had significantly enhanced Glu production, utilized in the CAC. This suggests that *STK11/Lkb1*-mutant cancers may benefit from glutaminase monotherapy, not currently recognized in the clinic. Currently, a phase II basket trial is investigating the efficacy of glutaminase inhibition (Telaglenastat) relative to mutations in *KEAP1*, *STK11/Lkb1*, or *NF1* to critically dissect efficacy relative to mutations of interest (NCT04265534). Our findings highlight the necessity of such trials to ensure the implementation of personalized therapeutic approaches.

Figure 6. Activated CD8 T cells require glutamine and glutaminase function to sustain antitumor activity

- (A) Expression of CD44 in CD8 T cells of representative vehicle/anti-PD1 (blue) and CB-839/anti-PD1 (red) tumor-bearing lungs.
- (B) Quantification of TCF1⁺ effector (E) and TCF1⁺ precursor (P) pool in activated (CD44⁺CD62L⁺) CD8 T cells in WT (n = 3), vehicle/isotype (n = 4); vehicle/anti-PD1 (n = 4); CB-839/isotype (n = 3); and CB-839/anti-PD1 (n = 4) tumor-bearing lungs. Two-way ANOVA E versus P: BL6 p = 0.0002; vehicle/anti-PD1 p = 0.0001.
- (C) Representative flow cytometry plots.
- (D) Quantification of IFN γ production (pg/mL) in SEB stimulated PBMCs treated with anti-PD1 (0.3 μ g/mL) or isotype control in a concentration gradient of glutamine (0–10 mM). Two-way ANOVA 0.37 mM p = 0.0042; 1.11, 3.33. and 10 mM p < 0.0001.
- (E) Expression of IFN γ and CD44 in CD8 T cells isolated from the spleens of representative vehicle/isotype, vehicle/anti-PD1, CB-839/isotype, and CB-839/anti-PD1 mice activated *ex vivo* with PMA/ionomycin for 6 h.
- (F) Quantification of IFN γ producing effector (CD44⁺CD8⁺) T cells isolated from the spleens of vehicle/isotype (n = 4); vehicle/anti-PD1 (n = 4); CB-839/isotype (n = 3); and CB-839/anti-PD1 (n = 4) mice. Unpaired t test CB-839 iso versus PD1 p = 0.0017.
- (G) Quantification of IFN γ , GzmB, and Ki67 expressing CD44⁺CD8⁺ effector T cell populations isolated from the tumor-bearing lungs of vehicle/isotype (n = 4); vehicle/anti-PD1 (n = 4); CB-839/isotype (n = 3); and CB-839/anti-PD1 (n = 4) mice activated *ex vivo* with PMA/ionomycin for 6 h. Unpaired t test IFN γ , vehicle iso versus PD1 p = 0.043; vehicle PD1 versus CB-839 PD1 p = 0.036; CB-839 iso versus PD1 p = 0.023; GzmB vehicle iso versus PD1 p = 0.039; vehicle PD1 versus CB-839 PD1 p = 0.037; Ki67 vehicle iso versus PD1 p = 0.021; and vehicle iso versus CB-839 PD1 p = 0.0096.

TCR-engaged CD8 T cells upregulate amino acid transporters and alter their metabolism from oxidative phosphorylation to glycolysis to support the bioenergetic requirements of activation and cytotoxicity (Carr et al., 2010; Sinclair et al., 2013). Indeed, metabolic rewiring is crucial for effector T cell functionality, and the impairment of this process hinders these responses essential for disease control (Macintyre et al., 2014; Yin et al., 2015). Gln is a conditionally essential amino acid and critical in both tumor and immune cell metabolism (Curthoys and Watford, 1995). Although activated T cells upregulate Gln transporters (SLC1A5, SLC38A2, and ASCT2) (Carr et al., 2010; Nakaya et al., 2014; Sinclair et al., 2013) and show signs of reliance on glutaminase activity (Johnson et al., 2018), Gln antagonism did not impede the activated phenotype in the context of subcutaneous *in vivo* tumors (Leone et al., 2019). However, glutaminase-deficient T cells *in vivo* failed to drive graft versus host inflammatory disease and cytotoxic T cells quickly exhausted (Johnson et al., 2018), suggesting distinct roles for Gln in T cell activation in different microenvironments. Consistent with these deficiencies, we show a significant reduction in the expansion of glutaminase-deficient CD8 T cells following a viral infection model, further highlighting the importance of glutaminase activity for CD8 T cell function in wide-ranging settings. We find that although the production of IFN γ by CD8 T cells increases with Gln availability, the enhanced activation afforded by anti-PD1 immunotherapy results in dependency on Gln availability in human PBMCs. Although previous studies have found that glutaminase inhibition using a variety of compounds (V-9302, 6-diazo-5-oxo-L-norleucine [DON], JHU-083) does not impact CD8 T cell activity *in vitro* (Byun et al., 2020), our findings clearly show that the requirement for glutaminase activity is pronounced following additional stimulation (immunotherapy). Critically, the combination of inhibiting both the PD1/PD-L1 axis and glutaminase enzymatic activity in T cells in the TME blunts their effector differentiation and cytotoxic capability.

Recently, inhibition of the PPP has caused similar controversy (Daneshmandi et al., 2021; Ghergurovich et al., 2020). The PPP diverts glucose-6-phosphate from the glycolytic pathway, initiated by the enzyme glucose-6-phosphate dehydrogenase (G6PD). We have previously shown that *KEAP1*-mutant lung adenocarcinomas are sensitive to PPP inhibition (Best et al., 2019), and here, we find that enhanced PPP metabolites are present in *Keap1*-deficient tumor nodules. However, in testing a G6PD inhibitor across many tumor and normal cell lines, T cells (MOLT-4, CD4⁺, CD8⁺, and Jurkat cell lines) were identified to be the most sensitive to inhibition (Ghergurovich et al., 2020). Furthermore, akin to glutaminase inhibition *in vivo*, G6PD inhibition decreased the cytotoxicity of CD8 T cells in *in vitro* assays (Ghergurovich et al., 2020). In contrast, in G6PD-deficient CD8 T cells, the metabolic changes were found to be advantageous to T cell metabolism and cytotoxicity (Daneshmandi et al., 2021). These studies suggest that investigating antitumor T cell cytotoxicity in immune-competent models is paramount to fully appreciate the complex interplay in the TME.

Therapeutic implications

These findings have significant clinical implications, given the emerging interest in harnessing the antitumor properties of glutaminase inhibition together with immunotherapy-induced im-

mune activation (Byun et al., 2020; Leone et al., 2019; Soth et al., 2020). Our studies highlight the importance of immune-competent murine models in oncoimmunology research and how they can serve as powerful model systems in examining the efficacy of combining glutaminase inhibition and immunotherapy. Critically, they enable the therapeutic effects of the tumor and immune cell compartments to be teased apart, providing valuable insights that may inform clinical trials (Olson et al., 2018). Notably, trials have been initiated to evaluate glutaminase inhibition in combination with immunotherapy (pembrolizumab or nivolumab) in patients with NSCLC (Phase I NCT03894540, terminated; Phase II NCT04265534, ongoing) and melanoma (NCT02771626, completed). Although no results from these trials have yet been released, information on the intratumoral T cell activation status from patients would be valuable to enhance our understanding of this phenomenon.

Limitations of the study

Through generating a cohort of *Keap1*- and/or *STK11*-/*Lkb1*-deficient *Kras*^{G12D} autochthonous lung adenocarcinoma models, the effects of co-mutation on metabolism and immunotherapy response were investigated. Although these GEMMs are widely accepted to be poorly immunogenic (DuPage and Jacks, 2013), they serve as unique *in vivo* model systems to interrogate the effect of combining glutaminase inhibition with immunotherapy. Although the combination therapy inhibited highly activated CD8 T cells and blunted their cytotoxic capabilities, the impact on overall survival was not evaluated. We cannot rule out the possibility that an altered dose or delivery schedule of CB-839 may yield a therapeutic window in which T cells can be activated to realize the functional synergy of glutaminase inhibitors with anti-PD1. Additionally, the complex TME in GEMMs, a pertinent reflection of the patient tumor, makes it difficult to say with certainty that the impact of glutaminase inhibition in the CD8 T cells alone was responsible for their impeded function, and not a result of the cross talk within cells of the TME. Finally, given that *KEAP1* and *STK11* mutant lung adenocarcinoma are generally associated with cigarette smoke and high tumor mutational burden (TMB) (Ricciuti et al., 2022; Skoulidis et al., 2015), it will be important to validate these findings in murine models engineered to exhibit a higher TMB and/or neoantigens (Fitzgerald et al., 2021; Westcott et al., 2021). Despite this, our findings suggest that glutaminase function must be unimpeded in CD8 T cells to ensure that they have the ability to reach their full cytotoxic potential.

STAR★METHODS

Detailed methods are provided in the online version of this paper and include the following:

- KEY RESOURCES TABLE
- RESOURCE AVAILABILITY
 - Lead contact
 - Materials availability
 - Data and code availability
- EXPERIMENTAL MODEL AND SUBJECT DETAILS
- METHOD DETAILS
 - Mice
 - Treatment studies

- Histology and immunohistochemistry
- Flow cytometry
- T cell activation assay
- LCMV expansion kinetics
- Quantitative RT-PCR
- RNA sequencing
- Metabolomic analyses

SUPPLEMENTAL INFORMATION

Supplemental information can be found online at <https://doi.org/10.1016/j.cmet.2022.04.003>.

ACKNOWLEDGMENTS

We are grateful to S. Oliver, L. Johnson, K. Hughes, and R. Monaghan for animal husbandry; L. Scott for genotyping; and S. Monard in the WEHI Flow Cytometry Facility and E. Tsui in the WEHI Histology Facility for expert support. Schematics were generated by P. Maltezos (WEHI) and using <https://biorender.com/>. Untargeted metabolomics analysis was performed at the Monash Proteomics and Metabolomics Facility. We are thankful to A.M. Pateron (Agiros Pharmaceuticals) and D.H. Gray (WEHI) for critical reading of the manuscript and useful discussions. This work was partially funded by a sponsored research agreement with Agios Pharmaceuticals and supported by an Australian National Health and Medical Research Council (NHMRC) Project Grant to K.D.S. (GNT1138275) and S.A.B. (GNT1159002) and a Priority-Driven Collaborative Cancer Research Scheme Grant funded by Cancer Australia to S.A.B. (2003127). K.D.S. is supported by a Victorian Cancer Agency Mid-Career Research Fellowship (18003) and the Peter and Julie Alston Centenary Fellowship. P.M.G. is supported by the Swiss National Foundation (P300PB_177934) and the Novartis Foundation for Medical-Biological Research, and J.A.M. is supported by a University of Melbourne Research Scholarship. This work was made possible through the Victorian Government Operational Infrastructure Support and Australian Government.

AUTHOR CONTRIBUTIONS

The experiments were conceived and designed by S.A.B., S.S., T.P.R., A.K., G.K., and K.D.S. Experiments were performed by S.A.B. with the assistance of A.K., P.M.G., S.S., J.A.M., and C.E.W. Bioinformatics analysis of RNA-seq was performed by W.A. and A.L.G. Metabolomics was performed by D.A., D.J.C., K.S., Y.L.N.A., J.G., and D.P. The manuscript was written by S.A.B. and K.D.S.

DECLARATION OF INTERESTS

This work was partially funded by a sponsored research agreement with Agios Pharmaceuticals. At the time the research was conducted, T. Roddy was employed by Agios Pharmaceuticals and had employee-related financial interests there. At the time of manuscript submission, T. Roddy was employed by Atavistik Bio and has no financial interests related to the work herein. D. Pirman is an employee and stockholder of Agios Pharmaceuticals and J. Goldford is a consultant for Agios Pharmaceutical and Atavistik Bio. K. Sutherland has received an Honorarium from Cygnal Therapeutics and direct research support from Pfizer Pharmaceuticals outside of the submitted work.

Received: October 12, 2021

Revised: January 28, 2022

Accepted: April 8, 2022

Published: May 2, 2022

REFERENCES

Armstrong, C., and Lillie, R.D. (1934). Experimental Lymphocytic Choriomeningitis of Monkeys and Mice Produced by a Virus Encountered in Studies of the 1933 St. Louis Encephalitis Epidemic. *Public Health Reports* 49, 1019–1027. <https://doi.org/10.2307/4581290>.

Bardeesy, N., Sinha, M., Hezel, A.F., Signoretti, S., Hathaway, N.A., Sharpless, N.E., Loda, M., Carrasco, D.R., and DePinho, R.A. (2002). Loss of the Lkb1 tumour suppressor provokes intestinal polyposis but resistance to transformation. *Nature* 419, 162–167. <https://doi.org/10.1038/nature01045>.

Barretina, J., Caponigro, G., Stransky, N., Venkatesan, K., Margolin, A.A., Kim, S., Wilson, C.J., Lehár, J., Kryukov, G.V., Sonkin, D., et al. (2012). The Cancer Cell Line Encyclopedia enables predictive modelling of anticancer drug sensitivity. *Nature* 483, 603–607. <https://doi.org/10.1038/nature11003>.

Best, S.A., De Souza, D.P., Kersbergen, A., Policheni, A.N., Dayalan, S., Tull, D., Rathi, V., Gray, D.H., Ritchie, M.E., McConville, M.J., and Sutherland, K.D. (2018a). Synergy between the KEAP1/NRF2 and PI3K pathways drives non-small-cell lung cancer with an altered immune microenvironment. *Cell Metab.* 27, 935–943.e4. <https://doi.org/10.1016/j.cmet.2018.02.006>.

Best, S.A., Ding, S., Kersbergen, A., Dong, X., Song, J.Y., Xie, Y., Reljic, B., Li, K., Vince, J.E., Rathi, V., et al. (2019). Distinct initiating events underpin the immune and metabolic heterogeneity of KRAS-mutant lung adenocarcinoma. *Nat. Commun.* 10, 4190. <https://doi.org/10.1038/s41467-019-12164-y>.

Best, S.A., Kersbergen, A., Asselin-Labat, M.L., and Sutherland, K.D. (2018b). Combining cell type-restricted adenoviral targeting with immunostaining and flow cytometry to identify cells-of-origin of lung cancer. *Methods Mol. Biol.* 1725, 15–29. https://doi.org/10.1007/978-1-4939-7568-6_2.

Best, S.A., and Sutherland, K.D. (2018). “Keaping” a lid on lung cancer: the Keap1-Nrf2 pathway. *Cell Cycle* 17, 1696–1707.

Blake, D.J., Singh, A., Kombairaju, P., Malhotra, D., Mariani, T.J., Tuder, R.M., Gabrielson, E., and Biswal, S. (2010). Deletion of Keap1 in the lung attenuates acute cigarette smoke-induced oxidative stress and inflammation. *Am. J. Respir. Cell Mol. Biol.* 42, 524–536. <https://doi.org/10.1165/rcmb.2009-0054OC>.

Byun, J.K., Park, M., Lee, S., Yun, J.W., Lee, J., Kim, J.S., Cho, S.J., Jeon, H.J., Lee, I.K., Choi, Y.K., and Park, K.G. (2020). Inhibition of glutamine utilization synergizes with immune checkpoint inhibitor to promote antitumor immunity. *Mol. Cell* 80, 592–606.e8. <https://doi.org/10.1016/j.molcel.2020.10.015>.

Cancer Genome Atlas Research Network (2014). Comprehensive molecular profiling of lung adenocarcinoma. *Nature* 511, 543–550. <https://doi.org/10.1038/nature13385>.

Carr, E.L., Kelman, A., Wu, G.S., Gopaul, R., Senkevitch, E., Aghvanyan, A., Turay, A.M., and Frauwirth, K.A. (2010). Glutamine uptake and metabolism are coordinately regulated by ERK/MAPK during T lymphocyte activation. *J. Immunol.* 185, 1037–1044. <https://doi.org/10.4049/jimmunol.0903586>.

Cerami, E., Gao, J., Dogrusoz, U., Gross, B.E., Sumer, S.O., Aksoy, B.A., Jacobsen, A., Byrne, C.J., Heuer, M.L., Larsson, E., et al. (2012). The cBio cancer genomics portal: an open platform for exploring multidimensional cancer genomics data. *Cancer Discov.* 2, 401–404. <https://doi.org/10.1158/2159-8290.CD-12-0095>.

Chalmers, Z.R., Connelly, C.F., Fabrizio, D., Gay, L., Ali, S.M., Ennis, R., Schrock, A., Campbell, B., Shlien, A., Chmielecki, J., et al. (2017). Analysis of 100,000 human cancer genomes reveals the landscape of tumor mutational burden. *Genome Med.* 9, 34. <https://doi.org/10.1186/s13073-017-0424-2>.

Chang, C.H., Qiu, J., O’Sullivan, D., Buck, M.D., Noguchi, T., Curtis, J.D., Chen, Q., Gindin, M., Gubin, M.M., van der Windt, G.J., et al. (2015). Metabolic competition in the tumor microenvironment is a driver of cancer progression. *Cell* 162, 1229–1241. <https://doi.org/10.1016/j.cell.2015.08.016>.

Chong, J., Soufan, O., Li, C., Caraus, I., Li, S., Bourque, G., Wishart, D.S., and Xia, J. (2018). MetaboAnalyst 4.0: towards more transparent and integrative metabolomics analysis. *Nucleic Acids Res.* 46, W486–W494. <https://doi.org/10.1093/nar/gky310>.

Clasquin, M.F., Melamud, E., and Rabinowitz, J.D. (2012). LC-MS data processing with MAVEN: a metabolomic analysis and visualization engine. *Curr. Protoc. Bioinformatics* 37, Unit14.11. <https://doi.org/10.1002/0471250953.bi1411s37>.

Corgnac, S., Malenica, I., Mezquita, L., Auclin, E., Voilin, E., Kacher, J., Halse, H., Grynspan, L., Signolle, N., Dayris, T., et al. (2020). CD103(+)CD8(+) TRM cells accumulate in tumors of anti-PD-1-Responder lung cancer patients and are tumor-reactive lymphocytes enriched with Tc17. *Cell. Reprod. Med.* 7, 100127. <https://doi.org/10.1016/j.xcrim.2020.100127>.

- Creek, D.J., Chua, H.H., Cobbold, S.A., Nijagal, B., MacRae, J.I., Dickerman, B.K., Gilson, P.R., Ralph, S.A., and McConville, M.J. (2016). Metabolomics-based screening of the malaria box reveals both novel and established mechanisms of action. *Antimicrob. Agents Chemother.* *60*, 6650–6663. <https://doi.org/10.1128/AAC.01226-16>.
- Cristescu, R., Mogg, R., Ayers, M., Albright, A., Murphy, E., Yearley, J., Sher, X., Liu, X.Q., Lu, H., Nebozhyn, M., et al. (2018). Pan-tumor genomic biomarkers for PD-1 checkpoint blockade-based immunotherapy. *Science* *362*, eaar3593. <https://doi.org/10.1126/science.aar3593>.
- Curthoys, N.P., and Watford, M. (1995). Regulation of glutaminase activity and glutamine metabolism. *Annu. Rev. Nutr.* *15*, 133–159. <https://doi.org/10.1146/annurev.nu.15.070195.001025>.
- Daneshmandi, S., Cassel, T., Lin, P., Higashi, R.M., Wulf, G.M., Boussiotis, V.A., Fan, T.W., and Seth, P. (2021). Blockade of 6-phosphogluconate dehydrogenase generates CD8(+) effector T cells with enhanced anti-tumor function. *Cell Rep.* *34*, 108831. <https://doi.org/10.1016/j.celrep.2021.108831>.
- DeNicola, G.M., Chen, P.H., Mullarky, E., Sudderth, J.A., Hu, Z., Wu, D., Tang, H., Xie, Y., Asara, J.M., Huffman, K.E., et al. (2015). NRF2 regulates serine biosynthesis in non-small cell lung cancer. *Nat. Genet.* *47*, 1475–1481. <https://doi.org/10.1038/ng.3421>.
- DuPage, M., Dooley, A.L., and Jacks, T. (2009). Conditional mouse lung cancer models using adenoviral or lentiviral delivery of Cre recombinase. *Nat. Protoc.* *4*, 1064–1072. <https://doi.org/10.1038/nprot.2009.95>.
- DuPage, M., and Jacks, T. (2013). Genetically engineered mouse models of cancer reveal new insights about the antitumor immune response. *Curr. Opin. Immunol.* *25*, 192–199. <https://doi.org/10.1016/j.coi.2013.02.005>.
- Fitzgerald, B., Connolly, K.A., Cui, C., Fagerberg, E., Mariuzza, D.L., Hornick, N.I., Foster, G.G., William, I., Cheung, J.F., and Joshi, N.S. (2021). A mouse model for the study of anti-tumor T cell responses in Kras-driven lung adenocarcinoma. *Cell Rep. Methods* *1*, 100080. <https://doi.org/10.1016/j.crmeth.2021.100080>.
- Galan-Cobo, A., Sitthideatphaiboon, P., Qu, X., Poteete, A., Pisegna, M.A., Tong, P., Chen, P.H., Boroughs, L.K., Rodriguez, M.L.M., Zhang, W., et al. (2019). LKB1 and KEAP1/NRF2 pathways cooperatively promote metabolic reprogramming with enhanced glutamine dependence in KRAS-mutant lung adenocarcinoma. *Cancer Res.* *79*, 3251–3267. <https://doi.org/10.1158/0008-5472.CAN-18-3527>.
- Gao, J., Aksoy, B.A., Dogrusoz, U., Dresdner, G., Gross, B., Sumer, S.O., Sun, Y., Jacobsen, A., Sinha, R., Larsson, E., et al. (2013). Integrative analysis of complex cancer genomics and clinical profiles using the cBioPortal. *Sci. Signal.* *6*, pii1. <https://doi.org/10.1126/scisignal.2004088>.
- Ghergurovich, J.M., García-Cañaveras, J.C., Wang, J., Schmidt, E., Zhang, Z., TeSlaa, T., Patel, H., Chen, L., Britt, E.C., Piqueras-Nebot, M., et al. (2020). A small molecule G6PD inhibitor reveals immune dependence on pentose phosphate pathway. *Nat. Chem. Biol.* *16*, 731–739. <https://doi.org/10.1038/s41589-020-0533-x>.
- Gross, M.I., Demo, S.D., Dennison, J.B., Chen, L., Chernov-Rogan, T., Goyal, B., Janes, J.R., Laidig, G.J., Lewis, E.R., Li, J., et al. (2014). Antitumor activity of the glutaminase inhibitor CB-839 in triple-negative breast cancer. *Mol. Cancer Ther.* *13*, 890–901. <https://doi.org/10.1158/1535-7163.MCT-13-0870>.
- Hallin, J., Engstrom, L.D., Hargis, L., Calinisan, A., Aranda, R., Briere, D.M., Sudhakar, N., Bowcut, V., Baer, B.R., Ballard, J.A., et al. (2020). The KRAS(G12C) inhibitor MRTX849 provides insight toward therapeutic susceptibility of KRAS-mutant cancers in mouse models and patients. *Cancer Discov.* *10*, 54–71. <https://doi.org/10.1158/2159-8290.CD-19-1167>.
- Im, S.J., Hashimoto, M., Gerner, M.Y., Lee, J., Kissick, H.T., Burger, M.C., Shan, Q., Hale, J.S., Lee, J., Nasti, T.H., et al. (2016). Defining CD8+ T cells that provide the proliferative burst after PD-1 therapy. *Nature* *537*, 417–421.
- Jackson, E.L., Olive, K.P., Tuveson, D.A., Bronson, R., Crowley, D., Brown, M., and Jacks, T. (2005). The differential effects of mutant p53 alleles on advanced murine lung cancer. *Cancer Res.* *65*, 10280–10288. <https://doi.org/10.1158/0008-5472.CAN-05-2193>.
- Jackson, E.L., Willis, N., Mercer, K., Bronson, R.T., Crowley, D., Montoya, R., Jacks, T., and Tuveson, D.A. (2001). Analysis of lung tumor initiation and progression using conditional expression of oncogenic K-ras. *Genes Dev.* *15*, 3243–3248. <https://doi.org/10.1101/gad.943001>.
- Ji, H., Ramsey, M.R., Hayes, D.N., Fan, C., McNamara, K., Kozlowski, P., Torrice, C., Wu, M.C., Shimamura, T., Perera, S.A., et al. (2007). LKB1 modulates lung cancer differentiation and metastasis. *Nature* *448*, 807–810. <https://doi.org/10.1038/nature06030>.
- Johnson, M.O., Wolf, M.M., Madden, M.Z., Andrejeva, G., Sugiura, A., Contreras, D.C., Maseda, D., Liberti, M.V., Paz, K., Kishton, R.J., et al. (2018). Distinct regulation of Th17 and Th1 cell differentiation by glutaminase-dependent metabolism. *Cell* *175*, 1780–1795.e19. <https://doi.org/10.1016/j.cell.2018.10.001>.
- Kallies, A., Zehn, D., and Utzschneider, D.T. (2020). Precursor exhausted T cells: key to successful immunotherapy? *Nat. Rev. Immunol.* *20*, 128–136. <https://doi.org/10.1038/s41577-019-0223-7>.
- Kerk, S.A., Papagiannakopoulos, T., Shah, Y.M., and Lyssiotis, C.A. (2021). Metabolic networks in mutant KRAS-driven tumours: tissue specificities and the microenvironment. *Nat. Rev. Cancer* *21*, 510–525. <https://doi.org/10.1038/s41568-021-00375-9>.
- Kim, J., Hu, Z., Cai, L., Li, K., Choi, E., Faubert, B., Bezwada, D., Rodriguez-Canales, J., Villalobos, P., Lin, Y.F., et al. (2017). CPS1 maintains pyrimidine pools and DNA synthesis in KRAS/LKB1-mutant lung cancer cells. *Nature* *546*, 168–172. <https://doi.org/10.1038/nature22359>.
- Koyama, S., Akbay, E.A., Li, Y.Y., Aref, A.R., Skoulidis, F., Herter-Sprie, G.S., Buczkowski, K.A., Liu, Y., Awad, M.M., Denning, W.L., et al. (2016). STK11/LKB1 deficiency promotes neutrophil recruitment and proinflammatory cytokine production to suppress T-cell activity in the lung tumor microenvironment. *Cancer Res.* *76*, 999–1008. <https://doi.org/10.1158/0008-5472.CAN-15-1439>.
- Lamberti, G., Spurr, L.F., Li, Y., Ricciuti, B., Recondo, G., Umeton, R., Nishino, M., Sholl, L.M., Meyerson, M.L., Cherniack, A.D., and Awad, M.M. (2020). Clinicopathological and genomic correlates of programmed cell death ligand 1 (PD-L1) expression in nonsquamous non-small-cell lung cancer. *Ann. Oncol.* *31*, 807–814. <https://doi.org/10.1016/j.annonc.2020.02.017>.
- Law, C.W., Chen, Y., Shi, W., and Smyth, G.K. (2014). voom: Precision weights unlock linear model analysis tools for RNA-seq read counts. *Genome Biol.* *15*, R29. <https://doi.org/10.1186/gb-2014-15-2-r29>.
- Lee, P.P., Fitzpatrick, D.R., Beard, C., Jessup, H.K., Lehar, S., Makar, K.W., Pérez-Melgosa, M., Sweetser, M.T., Schissel, M.S., Nguyen, S., et al. (2001). A critical role for Dnmt1 and DNA methylation in T cell development, function, and survival. *Immunity* *15*, 763–774. [https://doi.org/10.1016/S1074-7613\(01\)00227-8](https://doi.org/10.1016/S1074-7613(01)00227-8).
- Leone, R.D., Zhao, L., Englert, J.M., Sun, I.M., Oh, M.H., Sun, I.H., Arwood, M.L., Bettencourt, I.A., Patel, C.H., Wen, J., et al. (2019). Glutamine blockade induces divergent metabolic programs to overcome tumor immune evasion. *Science* *366*, 1013–1021. <https://doi.org/10.1126/science.aav2588>.
- Liao, Y., Smyth, G.K., and Shi, W. (2019). The R package Rsubread is easier, faster, cheaper and better for alignment and quantification of RNA sequencing reads. *Nucleic Acids Res.* *47*, e47. <https://doi.org/10.1093/nar/gkz114>.
- Liu, R., Holik, A.Z., Su, S., Jansz, N., Chen, K., Leong, H.S., Blewitt, M.E., Asselin-Labat, M.L., Smyth, G.K., and Ritchie, M.E. (2015). Why weight? Modelling sample and observational level variability improves power in RNA-seq analyses. *Nucleic Acids Res.* *43*, e97. <https://doi.org/10.1093/nar/gkv412>.
- Macintyre, A.N., Gerriets, V.A., Nichols, A.G., Michalek, R.D., Rudolph, M.C., Deoliveira, D., Anderson, S.M., Abel, E.D., Chen, B.J., Hale, L.P., and Rathmell, J.C. (2014). The glucose transporter Glut1 is selectively essential for CD4 T cell activation and effector function. *Cell Metab.* *20*, 61–72. <https://doi.org/10.1016/j.cmet.2014.05.004>.
- Mitsuishi, Y., Taguchi, K., Kawatani, Y., Shibata, T., Nukiwa, T., Aburatani, H., Yamamoto, M., and Motohashi, H. (2012). Nrf2 redirects glucose and glutamine into anabolic pathways in metabolic reprogramming. *Cancer Cell* *22*, 66–79. <https://doi.org/10.1016/j.ccr.2012.05.016>.
- Momcilovic, M., Bailey, S.T., Lee, J.T., Fishbein, M.C., Braas, D., Go, J., Graeber, T.G., Parlati, F., Demo, S., Li, R., et al. (2018). The GSK3 signaling axis regulates adaptive glutamine metabolism in lung squamous cell carcinoma. *Cancer Cell* *33*, 905–921.e5. <https://doi.org/10.1016/j.ccell.2018.04.002>.
- Nakaya, M., Xiao, Y., Zhou, X., Chang, J.H., Chang, M., Cheng, X., Blonska, M., Lin, X., and Sun, S.C. (2014). Inflammatory T cell responses rely on amino acid transporter ASCT2 facilitation of glutamine uptake and mTORC1 kinase

- activation. *Immunity* 40, 692–705. <https://doi.org/10.1016/j.immuni.2014.04.007>.
- Olson, B., Li, Y., Lin, Y., Liu, E.T., and Patnaik, A. (2018). Mouse models for cancer immunotherapy research. *Cancer Discov.* 8, 1358–1365. <https://doi.org/10.1158/2159-8290.CD-18-0044>.
- Papillon-Cavanagh, S., Doshi, P., Dobrin, R., Szustakowski, J., and Walsh, A.M. (2020). STK11 and KEAP1 mutations as prognostic biomarkers in an observational real-world lung adenocarcinoma cohort. *ESMO Open* 5, e000706. <https://doi.org/10.1136/esmoopen-2020-000706>.
- Papke, B., and Der, C.J. (2017). Drugging RAS: know the enemy. *Science* 355, 1158–1163. <https://doi.org/10.1126/science.aam7622>.
- Pearce, E.L., Poffenberger, M.C., Chang, C.H., and Jones, R.G. (2013). Fueling immunity: insights into metabolism and lymphocyte function. *Science* 342, 1242–1245. <https://doi.org/10.1126/science.1242454>.
- Phipson, B., Lee, S., Majewski, I.J., Alexander, W.S., and Smyth, G.K. (2016). Robust hyperparameter estimation protects against hypervariable genes and improves power to detect differential expression. *Ann. Appl. Stat.* 10, 946–963. <https://doi.org/10.1214/16-AOAS920>.
- Pierce, S.E., Granja, J.M., Corces, M.R., Brady, J.J., Tsai, M.K., Pierce, A.B., Tang, R., Chu, P., Feldser, D.M., Chang, H.Y., et al. (2021). LKB1 inactivation modulates chromatin accessibility to drive metastatic progression. *Nat. Cell Biol.* 23, 915–924. <https://doi.org/10.1038/s41556-021-00728-4>.
- Ricciuti, B., Arbour, K.C., Lin, J.J., Vajdi, A., Vokes, N., Hong, L., Zhang, J., Tolstorukov, M.Y., Li, Y.Y., Spurr, L.F., et al. (2022). Diminished efficacy of programmed death-(ligand)1 inhibition in STK11- and KEAP1-mutant lung adenocarcinoma is affected by KRAS mutation status. *J. Thorac. Oncol.* 17, 399–410. <https://doi.org/10.1016/j.jtho.2021.10.013>.
- Ritchie, M.E., Phipson, B., Wu, D., Hu, Y., Law, C.W., Shi, W., and Smyth, G.K. (2015). limma powers differential expression analyses for RNA-sequencing and microarray studies. *Nucleic Acids Res.* 43, e47. <https://doi.org/10.1093/nar/gkv007>.
- Rizvi, N.A., Hellmann, M.D., Snyder, A., Kvistborg, P., Makarov, V., Havel, J.J., Lee, W., Yuan, J., Wong, P., Ho, T.S., et al. (2015). Cancer immunology. Mutational landscape determines sensitivity to PD-1 blockade in non-small cell lung cancer. *Science* 348, 124–128. <https://doi.org/10.1126/science.aaa1348>.
- Robinson, M.D., McCarthy, D.J., and Smyth, G.K. (2010). edgeR: a Bioconductor package for differential expression analysis of digital gene expression data. *Bioinformatics* 26, 139–140. <https://doi.org/10.1093/bioinformatics/btp616>.
- Robinson, M.D., and Oshlack, A. (2010). A scaling normalization method for differential expression analysis of RNA-seq data. *Genome Biol.* 11, R25. <https://doi.org/10.1186/gb-2010-11-3-r25>.
- Romero, R., Sayin, V.I., Davidson, S.M., Bauer, M.R., Singh, S.X., LeBoeuf, S.E., Karakousi, T.R., Ellis, D.C., Bhutkar, A., Sánchez-Rivera, F.J., et al. (2017). Keap1 loss promotes Kras-driven lung cancer and results in dependence on glutaminolysis. *Nat. Med.* 23, 1362–1368. <https://doi.org/10.1038/nm.4407>.
- Saleh, M.M., Scheffler, M., Merkelbach-Bruse, S., Scheel, A.H., Ulmer, B., Wolf, J., and Buettner, R. (2022). Comprehensive analysis of TP53 and KEAP1 mutations and their impact on survival in localized- and advanced-stage NSCLC. *J. Thorac. Oncol.* 17, 76–88. <https://doi.org/10.1016/j.jtho.2021.08.764>.
- Sayin, V.I., LeBoeuf, S.E., Singh, S.X., Davidson, S.M., Biancur, D., Guzelhan, B.S., Alvarez, S.W., Wu, W.L., Karakousi, T.R., and Zavitsanou, A.M. (2017). Activation of the NRF2 antioxidant program generates an imbalance in central carbon metabolism in cancer. *Elife* 6, e28083.
- Sinclair, L.V., Rolf, J., Emslie, E., Shi, Y.B., Taylor, P.M., and Cantrell, D.A. (2013). Control of amino-acid transport by antigen receptors coordinates the metabolic reprogramming essential for T cell differentiation. *Nat. Immunol.* 14, 500–508. <https://doi.org/10.1038/ni.2556>.
- Singh, A., Daemen, A., Nickles, D., Jeon, S.M., Foreman, O., Sudini, K., Gnad, F., Lajoie, S., Gour, N., Mitzner, W., et al. (2021). NRF2 activation promotes aggressive lung cancer and associates with poor clinical outcomes. *Clin. Cancer Res.* 27, 877–888. <https://doi.org/10.1158/1078-0432.CCR-20-1985>.
- Singh, A., Happel, C., Manna, S.K., Acquah-Mensah, G., Carrerero, J., Kumar, S., Nasipuri, P., Krausz, K.W., Wakabayashi, N., Dewi, R., et al. (2013). Transcription factor NRF2 regulates miR-1 and miR-206 to drive tumorigenesis. *J. Clin. Invest.* 123, 2921–2934. <https://doi.org/10.1172/JCI66353>.
- Skoulidis, F., Byers, L.A., Diao, L., Papadimitrakopoulou, V.A., Tong, P., Izzo, J., Behrens, C., Kadara, H., Parra, E.R., Canales, J.R., et al. (2015). Co-occurring genomic alterations define major subsets of KRAS-mutant lung adenocarcinoma with distinct biology, immune profiles, and therapeutic vulnerabilities. *Cancer Discov.* 5, 860–877. <https://doi.org/10.1158/2159-8290.CD-14-1236>.
- Skoulidis, F., Goldberg, M.E., Greenawalt, D.M., Hellmann, M.D., Awad, M.M., Gainer, J.F., Schrock, A.B., Hartmaier, R.J., Trabucco, S.E., Gay, L., et al. (2018). STK11/LKB1 Mutations and PD-1 inhibitor resistance in KRAS-mutant lung adenocarcinoma. *Cancer Discov.* 8, 822–835. <https://doi.org/10.1158/2159-8290.CD-18-0099>.
- Skoulidis, F., and Heymach, J.V. (2019). Co-occurring genomic alterations in non-small-cell lung cancer biology and therapy. *Nat. Rev. Cancer* 19, 495–509. <https://doi.org/10.1038/s41568-019-0179-8>.
- Smyth, G.K., Michaud, J., and Scott, H.S. (2005). Use of within-array replicate spots for assessing differential expression in microarray experiments. *Bioinformatics* 21, 2067–2075. <https://doi.org/10.1093/bioinformatics/bti270>.
- Soth, M.J., Le, K., Di Francesco, M.E., Hamilton, M.M., Liu, G., Burke, J.P., Carroll, C.L., Kovacs, J.J., Bardenhagen, J.P., Bristow, C.A., et al. (2020). Discovery of IPN60090, a clinical stage selective Glutaminase-1 (GLS-1) inhibitor with excellent pharmacokinetic and physicochemical properties. *J. Med. Chem.* 63, 12957–12977. <https://doi.org/10.1021/acs.jmedchem.0c01398>.
- Sumner, L.W., Amberg, A., Barrett, D., Beale, M.H., Beger, R., Daykin, C.A., Fan, T.W., Fiehn, O., Goodacre, R., Griffin, J.L., et al. (2007). Proposed minimum reporting standards for chemical analysis chemical analysis working group (CAWG) metabolomics standards initiative (MSI). *Metabolomics* 3, 211–221. <https://doi.org/10.1007/s11306-007-0082-2>.
- Utzuschneider, D.T., Charmoy, M., Chennupati, V., Pousse, L., Ferreira, D.P., Calderon-Copete, S., Danilo, M., Alfei, F., Hofmann, M., Wieland, D., et al. (2016). T cell Factor 1-expressing memory-like CD8(+) T cells sustain the immune response to chronic viral infections. *Immunity* 45, 415–427. <https://doi.org/10.1016/j.immuni.2016.07.021>.
- Utzuschneider, D.T., Gabriel, S.S., Chisanga, D., Gloury, R., Gubser, P.M., Vasanthakumar, A., Shi, W., and Kallies, A. (2020). Early precursor T cells establish and propagate T cell exhaustion in chronic infection. *Nat. Immunol.* 21, 1256–1266. <https://doi.org/10.1038/s41590-020-0760-z>.
- Wang, J.B., Erickson, J.W., Fuji, R., Ramachandran, S., Gao, P., Dinavahi, R., Wilson, K.F., Ambrosio, A.L., Dias, S.M., Dang, C.V., and Cerione, R.A. (2010). Targeting mitochondrial glutaminase activity inhibits oncogenic transformation. *Cancer Cell* 18, 207–219. <https://doi.org/10.1016/j.ccr.2010.08.009>.
- Wang, R., Dillon, C.P., Shi, L.Z., Milasta, S., Carter, R., Finkelstein, D., McCormick, L.L., Fitzgerald, P., Chi, H., Munger, J., and Green, D.R. (2011). The transcription factor Myc controls metabolic reprogramming upon T lymphocyte activation. *Immunity* 35, 871–882. <https://doi.org/10.1016/j.immuni.2011.09.021>.
- Wang, Y., Bai, C., Ruan, Y., Liu, M., Chu, Q., Qiu, L., Yang, C., and Li, B. (2019). Coordinative metabolism of glutamine carbon and nitrogen in proliferating cancer cells under hypoxia. *Nat. Commun.* 10, 201. <https://doi.org/10.1038/s41467-018-08033-9>.
- Westcott, P., Muyas, F., Smith, O., Hauck, H., Sacks, N., Ely, Z., Jaeger, A., Rideout, W., Bhutkar, A., Zhang, D., et al. (2021). Mismatch repair deficiency is not sufficient to increase tumor immunogenicity. Preprint at bioRxiv. <https://doi.org/10.1101/2021.08.24.457572>.
- Wohlhieter, C.A., Richards, A.L., Uddin, F., Hulton, C.H., Quintanal-Villalonga, À., Martin, A., de Stanchina, E., Bhanot, U., Asher, M., Shah, N.S., et al. (2020). Concurrent mutations in STK11 and KEAP1 promote Ferroptosis protection and SCD1 dependence in lung cancer. *Cell Rep.* 33, 108444. <https://doi.org/10.1016/j.celrep.2020.108444>.
- Yin, Y., Choi, S.C., Xu, Z., Perry, D.J., Seay, H., Croker, B.P., Sobel, E.S., Brusko, T.M., and Morel, L. (2015). Normalization of CD4+ T cell metabolism reverses lupus. *Sci. Transl. Med.* 7, 274ra18. <https://doi.org/10.1126/scitranslmed.aaa0835>.

STAR★METHODS

KEY RESOURCES TABLE

REAGENT or RESOURCE	SOURCE	IDENTIFIER
Antibodies		
EpCAM	Biologend	RRID: AB_1501158
CD45	Biologend	RRID: AB_312979
CD3	Biologend	RRID: AB_312670
PD-L1	Biologend	RRID: AB_10897097
PD-1	Biologend	RRID: AB_11125371
CD4	Biologend	RRID: AB_493701
FoxP3	Biologend	RRID: AB_439749
CD11c	Biologend	RRID: AB_313778
CD11b	Biologend	RRID: AB_312788
Ly6G	Biologend	RRID: AB_1186105
CD103	Biologend	RRID: AB_535948
CD44	Biologend	RRID: AB_493712
CD62L	Biologend	RRID: AB_830798
Ki67	Biologend	RRID: AB_2562664
TIM3/CD366	Biologend	RRID: AB_2571932
TCF1/TCF7	Cell Signaling	RRID: AB_2797631
LAMP/CD107a	Biologend	RRID: AB_2565965
CD25	Biologend	RRID: AB_2562270
ICOS	eBioscience	RRID: AB_2744728
Granzyme B	Biologend	RRID: AB_2728384
IFN gamma	Biologend	RRID: AB_11142685
CD8a	Synaptic Systems	RRID: AB_2620121
CD45	BD Biosciences	RRID: AB_394606
FoxP3	eBioscience	RRID: AB_467576
Ly5.2	BD Bioscience	RRID: AB_560697
Ly5.1	BD Bioscience	RRID: AB_558701
PD-1	BioXCell	RRID: AB_10949053
Rat IgG2a	BioXCell	RRID: AB_2687732
IOTest Beta Mark kit	Beckman Coulter	Cat# PIM3497
Bacterial and virus strains		
Adenovirus: Ad5-CMV-Cre	University of Iowa Gene Transfer Core Facility	Cat# VVC-U of Iowa-5
Lymphocytic choriomeningitis virus, strain Armstrong	Armstrong and Lillie, 1934	N/A
Chemicals, peptides, and recombinant proteins		
CB-839	BLDpharm	Cat# BD303413
staphylococcal enterotoxin B (SEB)	Sigma-Aldrich	Cat# S4881
L-Glutamine	Sigma-Aldrich	Cat# 59202C
Phorbol myristate acetate (PMA)/Ionomycin with Brefeldin-A	Sigma-Aldrich	Cat# 423303
L-Glutamine- ¹³ C ₅ , ¹⁵ N ₂	Sigma-Aldrich	Cat# 607983
Deposited data		
RNA-seq: <i>Kras</i> -mutant mouse tumor models	This paper	GEO: GSE193895
Metabolomics: steady-state LC-MS analysis of <i>Kras</i> -mutant mouse tumor models	This paper	Metabolomics Workbench https://doi.org/10.21228/M8N98X

(Continued on next page)

Continued		
REAGENT or RESOURCE	SOURCE	IDENTIFIER
Metabolomics: steady-state and glutamine-labeling LC-MS of KL and KKL tumor models	This paper	Mendeley Data https://doi.org/10.17632/6rdzdp624.1
Raw data to generate all graphs of the paper	This paper	Data S1
Experimental models: Organisms/strains		
Mouse: <i>Keap1</i> ^{f/f}	Dr. Shyam Biswal, JHSPH	N/A
Mouse: <i>Kras</i> ^{G12D}	The Jackson Laboratory	LSL-K-ras G12D; B6.129S4-Kras ^{tm1Tyj} /J,
Mouse: <i>Lkb1</i> ^{f/f}	The Jackson Laboratory	B6.129S4- <i>Stk11</i> ^{tm1.1Sjm} /J
Mouse: <i>p53</i> ^{f/f}	The Jackson Laboratory	B6.129P2- <i>Trp53</i> ^{tm1Bm} /J
Mouse: P14 TCR transgene	The Jackson Laboratory	Tg(TcrLCMV)327Sdz
Mouse: CD4Cre	Lee et al., 2001	N/A
Mouse: <i>Gls1</i> ^{f/f}	Dr. Jeffrey Rathmell, Vanderbilt	Glstm1a(KOMP)Mbp KOMP Project ID: CSD29307
Oligonucleotides		
Genotyping primers – <i>Keap1</i> 5'-CGAGGAAGCGTTTGCTTTAC- 3', 5'- GAGTCACCGTAAGCCT GGTC-3'	Blake et al., 2010	N/A
Genotyping primers – <i>Kras</i> ^{G12D} 5'- CGCAGACTGTAGAGCAG CG -3', 5'- CCATGGCTTGAGTAAGTCTGC -3'	The Jackson Laboratory	N/A
Genotyping primers – <i>p53</i> 5'- AAGGGGTATGAGGGACA AGG -3', 5'- GAAGACAGAAAAGGGGAGGG -3'	The Jackson Laboratory	N/A
Genotyping primers – <i>Lkb1</i> 5'- ATCGGAATGTGATCCAGCTT - 3', 5'- ACGTAGGCTGTGCAACCTCT -3'	The Jackson Laboratory	N/A
Genotyping – P14 TCR transgene 5'- CATGGAGGCTGCAGTC ACCC -3', 5'- GTTTGTTTGC GAGCTCTGTTTGATGGCTC -3' 5'- CAAATGTTGCTTGCTG GTG -3' 5'- GTCAGTCGAGTG CAC AGT TT -3'	The Jackson Laboratory	N/A
Genotyping – <i>Gls1</i> 5'- GAGA TGGCGCAACGCAATTAATG -3' 5'- GCACA TGCATACTACATGACACTAAAGC -3' 5'- TAAGTCTGTGGCTGGTCTCCAGG -3' 5'- ACAATGTACCTGAGGGAGTTGACAGG -3'	Johnson et al., 2018	N/A
Genotyping – CD4Cre 5'- CTAGGCCACAGAATTGAAAGATCT -3' 5'- GCGGTCTGGCAGTAAAACTATC -3' 5'- GTAGGTGAAAATTCTAGCATCATCC -3' 5'- GTGAAACAGCATTGCTGCTCACTT -3'	Lee et al., 2001	N/A
Quantitative RT-PCR primers – <i>Gapdh</i> 5'- GCCAAGGTCATCCATGACAACT-3', 5'- GAGGGGCCATCCACAGTCTT-3'	Best and Sutherland, 2018	N/A
Quantitative RT-PCR primers – <i>Gls1</i> 5'- TTCGCCCTCGGAGATCCTAC -3', 5'- CCAAGCTAGGTAACAGACCCT -3'	Primer bank	164607131c1
Software and algorithms		
GraphPad Prism 7	GraphPad Software	http://www.graphpad.com/scientific-software/prism/
Zen	Zeiss	https://www.zeiss.com/microscopy/int/products/microscope-software/zen.html

(Continued on next page)

Continued

REAGENT or RESOURCE	SOURCE	IDENTIFIER
FlowJo	FlowJo LLC	https://www.flowjo.com/solutions/flowjo
Image J	Softonic	https://imagej.net/Welcome
cBioPortal for Cancer Genomics	Cerami et al., 2012; Gao et al., 2013	http://www.cbioportal.org/
IDEOM software	Creek et al., 2016	http://mzmatch.sourceforge.net/ideom.php
MetaboAnalystR software	Chong et al., 2018	https://www.metaboanalyst.ca/
R version 4.0.5	R software	https://www.r-project.org/
Bioconductor version 3.14 packages	Bioconductor	https://www.bioconductor.org/

RESOURCE AVAILABILITY

Lead contact

- Further information and requests for resources and reagents should be directed to and will be fulfilled by the lead contact, Kate Sutherland (sutherland.k@wehi.edu.au).

Materials availability

- Mouse crosses generated in this study are available upon reasonable request, MTA restrictions may apply.

Data and code availability

- RNA-seq data have been deposited at GEO and metabolomics data have been deposited at Metabolomics Workbench and Mendely Data. Data are publicly available as of the date of publication and accession numbers are listed in the [key resources table](#). All values used to generate the graphs displayed in the paper can be found in [Data S1 – Source Data](#).
- This paper does not report original code.
- Any additional information required to reanalyze the data reported in this paper is available from the lead contact upon request.

EXPERIMENTAL MODEL AND SUBJECT DETAILS

All experiments presented in this study were conducted according to regulatory standards approved by the Walter and Eliza Hall Institute and University of Melbourne Animal Ethics Committees. An equal proportion of males and females were used in all experiments and all mice were maintained on a pure C57BL/6 background. At 7-8 weeks old, littermates were randomized into Ad5-CMV-Cre infected, or uninfected, and when relevant were randomly assigned into treatment arms, distributed evenly by litter and sex. Mice were housed within these groups for the latency of the experiment under a 12-hour light/dark cycle. All animals were used in scientific experiments for the first time. This includes no previous exposures to pharmacological substances. Health status was normal for all animals.

METHOD DETAILS

Mice

We conducted all animal experiments according to regulatory standards approved by the Walter and Eliza Hall Institute and University of Melbourne Animal Ethics Committees. *Keap1^{flox}* mice (Blake et al., 2010) mice were a generous gift from S. Biswal (John Hopkins Bloomberg School of Public Health). *Kras^{G12D/+}*, *p53^{flox}* mice (Jackson et al., 2005) and *Lkb1^{flox}* mice (Bardeesy et al., 2002) have been previously described, with *Gls1^{flox}* mice (Johnson et al., 2018) and *CD4Cre* mice (Lee et al., 2001) crossed to include the P14 TCR transgene (JAX: Tg(TcrLCMV)327Sdz). Wild-type C57Bl/6JArc mice on a Ly5.1 background were obtained from the Australian Resources Center. All animals were maintained on a pure C57Bl/6 background, and equal proportions of males and females were used in all experiments. Mice were genotyped using primers outlined in the [key resources table](#). Seven-to-eight-week old conditional mice were intranasally (i.n) infected with 20 μ l of 1×10^{10} PFU/ml Ad5-CMV-Cre virus (University of Iowa Gene Transfer Core Facility) according to standard procedures (DuPage et al., 2009). At defined timepoints (K: 90 days, KK: 60 days, KL and KKL: 40 days post Ad5-CMV-Cre), mice were sacrificed by cardiac puncture and lungs and other organs harvested for downstream analysis.

Treatment studies

For anti-PD1 survival study, 20 days following Ad5-CMV-Cre, KL and KKL mice were randomly assigned to anti-PD1 or isotype control antibody (200 μ g RMP1-14 or Rat IgG2a; BioXCell) treatment arms (n = 6/arm). Each cycle (every 20 days) consisted of intra-peritoneal injection (200 μ l into left and right flank) three times over 6 days (day 0, 3, 6). Mice were collected at ethical endpoint for Kaplan

Meier survival analysis. For combination anti-PD1/CB-839 study, 20 days following Ad5-CMV-Cre, KL mice were randomly assigned to vehicle/isotype, vehicle/anti-PD1, CB-839/isotype or CB-839/anti-PD1 treatment arms (study 1: $n = 6/\text{arm}$; study 2: $n = 4/\text{arm}$). On day 20, mice received one cycle of anti-PD1 or isotype control (as above) and 200 mg/kg CB-839 (2 % w/v CB-839; BLDpharm, in vehicle) or vehicle (20 % Solutol HS15 / 20 % SB- β -CD (Captisol) / 50 mM phosphate buffer, pH 7.4) twice daily by oral gavage until collection on day 29, when mice were collected 12 hours following the final dose. At harvest, mice were sacrificed by cardiac bleed and the left lung lobe was weighed and processed for flow cytometry with spleens, while right lung lobes were inflated with 4 % paraformaldehyde and processed for histology.

Histology and immunohistochemistry

Lungs were perfused and fixed in 4 % paraformaldehyde for 24 hours at 4 °C and embedded in paraffin. Sections 2 μm thick were stained with hematoxylin and eosin (H&E) and sections 4 μm thick were immunostained. Slides were dewaxed in xylene, re-hydrated and exposed to antigen retrieval using pH 6.0 Citrate buffer (1.8 mM citric acid, 8.2 mM sodium citrate) in a DAKO pressure cooker (125 °C 30 sec). Endogenous peroxidase activity was quenched using 3 % Hydrogen Peroxide, 5 min. Sections were blocked in 5 % goat serum and washed in 0.05 % Tween20/PBS. Primary antibodies ([key resources table](#)) were incubated overnight at 4 °C in a humidifier box. For immunohistochemistry, biotinylated secondary antibodies and Vectastain Elite ABC HRP reagent (Vector Laboratories PK-7100) were each incubated for 30 min at RT. ImmPACT DAB Peroxidase substrate (Vector Laboratories SK-4105) was used according to manufacturer's instructions, and sections counterstained (15 sec hematoxylin, 30 sec schotts tap water) and coverslipped. Slides were imaged using Nikon Eclipse 50i microscope with Axiovision software (Zeiss). CD8 T cells were quantified in tumor regions using the measure tool on Image J software (Softonic).

Flow cytometry

Single cell suspensions of the lung were generated as described in detail previously ([Best et al., 2018b](#)). Spleens were passed through a 100 μm sieve and red blood cells lysed in 0.8 % NH_4Cl (Sigma A4514) for 3 min at RT. Samples were blocked in FcR blocking reagent (Milteny Biotech 130-092-575) and 0.1 mg/mL Rat IgG for 15 min at 4 °C. Primary antibodies ([key resources table](#)) were incubated for 30 min at 4 °C. Intracellular stains were performed using the eBioscience Transcription Factor Staining Buffer Set (Thermo Scientific 00-5523-00). Staining for Granzyme B (GzmB) and $\text{IFN}\gamma$ was performed on single cell suspensions that were stimulated with ionomycin (0.1 $\mu\text{g}/\text{mL}$) and phorbol myristate acetate (PMA, 0.1 $\mu\text{g}/\text{mL}$) for 6 hours at 37 °C. Unstimulated cells incubated at 37 °C for 6 hours were used as a negative control. TCR V β clonotype repertoires were analyzed using the IOTest Beta Mark kit (Beckman Coulter PIM3497). Analysis was performed on the LSR II flow cytometer (BD Biosciences) or Aurora spectral unmixing cytometer (CyTEK). All data was analyzed using FlowJo software (FlowJo LLC). Multidimensional tSNE plots were generated using the DownSample plugin with tSNE function on FlowJo.

T cell activation assay

The staphylococcal enterotoxin B (SEB) assay was performed on peripheral blood mononuclear cells (PBMC) isolated from whole human blood by density gradient centrifugation. PBMC were pre-stained with Celltrace violet and incubated with or without 0.3 $\mu\text{g}/\text{mL}$ anti-PD1 for 1 hour. Treated PBMCs were plated at 1×10^5 cells/well in 96-well assay plates and stimulated with 5 ng/mL SEB with Glutamine titration (10, 3.33, 1.11, 0.37, 0.12, 0.04, 0.01, 0 mM) in media with 5 mM glucose and 10 % FBS. After 4 days, $\text{IFN}\gamma$ was detected by ELISA assay.

LCMV expansion kinetics

Single-cell splenocyte suspensions were obtained by passing total spleens through a 70 μm nylon cell strainer (BD), and red blood cells were lysed with a hypotonic ammonium chloride–potassium bicarbonate buffer. Transgenic naive P14 T cells ($\text{Gls}1^{+/+}; \text{CD4Cre}$ or $\text{Gls}1^{\text{fl/fl}}; \text{CD4Cre}$) were isolated using the mouse CD8⁺ T cell enrichment kit (Milteny Biotech), and 2×10^4 P14 T cells were intravenously injected into naive congenically marked recipients. On the following day, Ly5.1 recipient mice were infected intraperitoneally with 2×10^5 PFU of LCMV Armstrong. Blood from mice was obtained with submandibular bleeds on days 6 and 13 after infection and percentages of P14 cells among all CD8 T cells was assessed with congenic markers by flow cytometry.

Quantitative RT-PCR

RNA was extracted from ground tumor tissue using the RNeasy RNA extraction kit (Qiagen 74104), followed by the SuperScript III kit (Thermo Fisher 18080051). Quantitative RT-PCR was performed using SyberGreen (Bioline QT605-05) on the Vii7 Real-Time PCR System (Thermo Scientific). Relative mRNA was calculated compared to *Gapdh* internal control using the delta-delta-cT statistical method ([key resource table](#)).

RNA sequencing

Snap frozen tumors ($n = 5$ mice / 2 tumors per mouse) or uninfected littermate control lung ($n = 6$) were ground in liquid nitrogen and RNA extracted using the RNeasy RNA extraction kit (Qiagen 74104) then analyzed using a 2200 TapeStation Analyser (Agilent). An input of 150 ng RNA was used to generate libraries (TruSeq RNA Library Prep v2, Illumina). Sequencing was performed on the NextSeq System (Illumina) to produce 80bp paired-end reads. Between 13 and 76 million reads were generated for each sample and reads were aligned to the *Mus musculus* genome (mm10) using Rsubread ([Liao et al., 2019](#)). Aligned reads were processed

by Rsubread's featureCounts function using GENCODE Release M24 (GRCm38.p6) annotation to count the number of reads overlapping each annotated gene. Low expressed genes were filtered out using edgeR's (Robinson et al., 2010) filterByExpr function. Genes without annotation were also filtered. Differential expression (DE) analyses were undertaken using the edgeR and limma (Ritchie et al., 2015) software packages. Library sizes were normalized using the trimmed mean of M-values (TMM) method (Robinson and Oshlack, 2010). Sample quality weights were estimated using voomWithQualityWeights (Liu et al., 2015) and differential expression was evaluated using voom (Law et al., 2014) with robust empirical Bayes estimation of the variances (Phipson et al., 2016). Correlations between repeated measurements (multiple tumour samples) from the same mouse were estimated using the duplicateCorrelation method (Smyth et al., 2005). The false discovery rate (FDR) was controlled below 0.05 using the method of Benjamini and Hochberg.

Metabolomic analyses

Steady state analysis

Blood (100 μ L) was collected at defined time points by mandible bleed into a lithium-heparin micro tube (Sarstedt 41.1393.005). After centrifugation (13,000 g, 4 $^{\circ}$ C, 10 min) plasma was transferred to Eppendorf tubes and snap-frozen for metabolite analysis. 25 μ L of plasma was extracted with 100 μ L of cold MeOH and shaken in a cool room for 1 hour. The extracts were centrifuged at 4 $^{\circ}$ C at 14.8 g for 10 min, supernatant transferred to LCMS vials. 10 μ L injected for metabolomics analysis.

Tumor tissue was flash frozen and crushed using a mortar and pestle in liquid nitrogen. To the Eppendorf tubes 150 μ L of cold 80 % acetonitrile was added and vortexed quickly. The suspension was transferred to a fresh Eppendorf tube. Another 150 μ L portion of extraction solvent was added to the tubes, vortexed and the suspension combined with the first portion. To the combined extraction mixture 75 μ L of CHCl_3 was added and samples were mixed for 1 h in a cool room to ensure complete extraction. The samples were centrifuged at 4 $^{\circ}$ C at 14.8 g for 10 min, supernatant transferred to new tubes and evaporated at 20 $^{\circ}$ C under a stream of nitrogen. BSA assay was performed on the protein pellet by dissolving all protein in equal volume of detergent solution (4 % v/v SDS in water). Dried samples were resolubilized in appropriate volume of CHCl_3 : MeOH : H_2O (1 : 3 : 1, v/v) mixture based on measured protein content, shaken for 15 min at room temperature, centrifuged at 4 $^{\circ}$ C at 14.8 g for 10 min. 100 μ L of the supernatant was transferred to LCMS vials. 10 μ L injected for metabolomics analysis.

LCMS analysis was performed on QExactive mass spectrometer coupled with Dionex Uimate3000RS LCMS system (Thermo Fisher Scientific, Waltham, Massachusetts, USA) and data processing was performed using IDEOM software as described previously (Creek et al., 2016). Metabolites were putatively annotated based on accurate mass and predicted retention time by the IDEOM software (Metabolite Standards Initiative: MSI level 2). The identities of common metabolites, including glutamine, glutamate, aspartate, glutathione, ribose, IMP, orotate and dihydroorotate, were confirmed by mass and retention time alignment with authentic standards analyzed in the same batch (MSI level 1) (Sumner et al., 2007). Results were expressed as data matrices, where peak height were reported for putatively identified metabolites in all the samples and analyzed using MetaboAnalystR software (Chong et al., 2018).

Glutamine tracing analysis

KL and KKL tumor-bearing mice and uninfected littermates (UN) ($n = 5/\text{arm}$) received intra-peritoneal injection of 14.4 mg $\text{U-}^{13}\text{C, U-}^{15}\text{N}$ -glutamine (Sigma-Aldrich), 15 minutes prior to mandible bleed (into lithium/heparin tube) and sacrifice. Tumor pieces or normal lung tissue ($n = 4/\text{mouse}$) were immediately harvested into Eppendorf tubes and flash-frozen in liquid nitrogen for metabolomics analysis. Tissue pieces were homogenized to powder using Covaris CP02 tissue pulverizer (Covaris, Woburn, MA). Tissue was weighed and extracted using 80/20 methanol/water at -20 $^{\circ}$ C at a ratio of 40 μ L/mg tissue. Samples were vortexed, centrifuged and supernatant evaporated using a Genevac (SP Scientific, Warminster, PA). Plasma samples were thawed and 10 μ L were aliquoted and extracted with 90 μ L of 80/20 methanol/water at -20 $^{\circ}$ C. Samples were vortexed, centrifuged and supernatant evaporated using a Genevac. Samples were reconstituted in water for metabolite analysis. Positive and negative mode metabolite analyses were performed with reversed-phase ion-pairing liquid chromatography mass spectrometry (LC-MS) on a Thermo Vanquish Flex pump coupled to a QExactive orbitrap mass spectrometer using electrospray ionization (Thermo Fisher Scientific, San Jose, CA). Chromatography for negative mode ionization, the stationary phase was an ACQUITY UPLC HSS T3 (1.8 μm 2.1x150 mm) column. LC separation was achieved with a gradient elution of solvent A (97/3 H_2O /methanol with 10 mM tributylamine, 15 mM acetic acid at a pH of 4.9), and solvent B (methanol). The gradient was 0 min, 0 % B; 3 min, 20 % B; 5.5 min, 20 % B; 11 min, 55 % B; 13.5 min, 95 % B; 16.5 min, 95 % B; 17 min, 0 % B. The flow rate was 200 μ L/min. Positive mode LC separation was achieved with a gradient of solvent A (0.025 % heptafluorobutyric acid, 0.1 % formic acid in H_2O) and solvent B (acetonitrile) at 400 μ L/min. The stationary phase was an Waters Atlantis T3, 3 μm , 2.1 mm x 150 mm column. The gradient was 0 min, 0 % B; 4 min, 30 % B; 6 min, 35 % B; 6.1 min, 100 % B; 7 min, 100 % B; 7.1 min, 0 % B. For both ionization modes, the injection volume was 10 μ L and the QExactive Mass Spectrometer scanned in negative mode from m/z 70-1,000 at a resolving power of 70,000.

Metabolites were identified by matching exact mass and retention time to external standards. Area counts for each metabolite's abundance and associated isotopologues were quantified by EI-MAVEN (Elucidata Inc) (Clasquin et al., 2012). Correction for the natural abundance of carbon was performed with an in-house software LC-MS Data Processor. Fractional enrichment (FE) was calculated by dividing the area of an isotopologue by the sum of areas of all isotopologues for each metabolite. Results were expressed as data matrices, where peak height were reported for putatively identified metabolites in all the samples and analyses performed using MetaboAnalystR software (Chong et al., 2018).

TCGA and CCLE data analysis

RNA-seq read counts and mutations status for lung adenocarcinomas from The Cancer Genome Atlas (TCGA) project ([Cancer Genome Atlas Research Network, 2014](#)) or Cancer Cell Line Encyclopedia (CCLE) ([Barretina et al., 2012](#)) were interrogated using cBioPortal publicly available software ([Cerami et al., 2012](#); [Gao et al., 2013](#)).

Statistical analysis

Statistical analysis was performed using Prism software (GraphPad Software). Pairwise comparisons were performed using an unpaired Student *t* test and multivariate comparisons were performed using one-way ANOVA (Kruskal-Wallis test) with Tukey's multiple comparisons test or two-way ANOVA with Dunn's multiple comparisons test for grouped analyses.